Monthly Notices
of the
ROYAL ASTRONOMICAL SOCIETY

MNRAS **505,** 259–273 (2021)
Advance Access publication 2021 May 4

doi:10.1093/mnras/stab1264

Virial shocks are suppressed in cosmic ray-dominated galaxy haloes

Suoqing Ji [1]★ Dušan Kereš,[2] T. K. Chan [2,3] Jonathan Stern [4] Cameron B. Hummels,[1]
Philip F. Hopkins [1] Eliot Quataert [5,6] and Claude-André Faucher-Giguère [4]

[1]*TAPIR, Mailcode 350-17, California Institute of Technology, Pasadena, CA 91125, USA*
[2]*Department of Physics, Center for Astrophysics and Space Sciences, University of California at San Diego, 9500 Gilman Drive, La Jolla, CA 92093, USA*
[3]*Institute for Computational Cosmology, Durham University, South Road, Durham DH1 3LE, UK*
[4]*Department of Physics and Astronomy and CIERA, Northwestern University, 2145 Sheridan Road, Evanston, IL 60208, USA*
[5]*Department of Astronomy and Theoretical Astrophysics Center, University of California Berkeley, Berkeley, CA 94720, USA*
[6]*Department of Astrophysical Sciences, 4 Ivy Lane, Princeton University, Princeton, NJ 08544, USA*

Accepted 2021 April 28. Received 2021 April 5; in original form 2020 November 7

ABSTRACT

We study the impact of cosmic rays (CRs) on the structure of virial shocks, using a large suite of high-resolution cosmological FIRE-2 simulations accounting for CR injection by supernovae. In Milky Way-mass, low-redshift ($z \lesssim 1-2$) haloes, which are expected to form 'hot haloes' with slowly cooling gas in quasi-hydrostatic equilibrium (with a stable virial shock), our simulations without CRs do exhibit clear virial shocks. The cooler phase condensing out from inflows becomes pressure confined to overdense clumps, embedded in low-density, volume-filling hot gas with volume-weighted cooling time longer than inflow time. The gas thus transitions sharply from cool free-falling inflow, to hot and thermal-pressure supported at approximately the virial radius ($\approx R_{\rm vir}$), and the shock is quasi-spherical. With CRs, we previously argued that haloes in this particular mass and redshift range build up CR-pressure-dominated gaseous haloes. Here, we show that when CR pressure dominates over thermal pressure, there is no significant virial shock. Instead, inflowing gas is gradually decelerated by the CR pressure gradient and the gas is relatively subsonic out to and even beyond $R_{\rm vir}$. Rapid cooling also maintains subvirial temperatures in the inflowing gas within $\sim R_{\rm vir}$.

Key words: stars: formation – galaxies: active – galaxies: evolution – galaxies: formation – cosmology: theory.

1 INTRODUCTION

The thermal evolution of accreted gas on to galaxies is one of the essential processes shaping galaxy formation. In the classic scenario, initially cold gas from the intergalactic medium (IGM) is shock heated when falling into dark matter (DM) haloes, and reaches quasi-hydrodynamical equilibrium at a virial temperature $T_{\rm vir} \sim 10^6 (V_c/167\,{\rm km\,s^{-1}})^2$, where V_c is the circular velocity. After that, hot gaseous haloes start to cool from inside out; the inner region contracts quasi-statically and feeds on to galactic discs as the fuel for star formation (Rees & Ostriker 1977; White & Rees 1978; Fall & Efstathiou 1980). Birnboim & Dekel (2003) explore this scenario into further details by carrying out an analytic study with 1D spherical hydrodynamic simulations, where the stability of radiative shocks in gas falling into DM haloes is investigated. It is shown that when cooling is inefficient, the incoming gas accelerated by the DM gravitational potential accretes supersonically and evolves into shocks as the gas piles up. The post-shock regions become thermalized and provide thermal pressure support for newly accreted gas, and therefore a stable virial shock front can form at virial radius $R_{\rm vir}$. In contrast, when cooling is efficient, the post-shock regions rapidly radiates away its thermal energy and cannot support a stable shock front. A general condition for stable virial shocks is when the local gas cooling time-scale is greater than the gas compression time, which corresponds to a critical halo mass greater than $\sim 10^{11.5}\,{\rm M}_\odot$ with a metallicity of $\sim 0.05 {\rm Z}_\odot$ (Dekel & Birnboim 2006). As a result, in massive haloes of $M_{\rm halo} \gtrsim 10^{11.5}\,{\rm M}_\odot$, gas is shock heated after entering galaxy haloes and ultimately accreted on to galaxies.

However, various complications emerge when spherical-symmetry is broken or heating by feedback is included. A number of multidimensional numerical simulations have extended this picture of gas accretion to account for three-dimensional effects important in a realistic cosmological environment: cold gas can possibly accrete in the form of anisotropic filamentary inflows that penetrate hot halo gas and feed galaxies directly (Kereš et al. 2005). Therefore, there might exist two distinct regimes for gas accretion in DM haloes, the 'cold' mode in low-mass haloes and the 'hot' mode in high-mass ones at low redshifts respectively. At high redshift, one can have efficient cold mode accretion even in massive haloes that are dominated by hot virialized atmospheres (e.g. Kereš et al. 2005, 2009). A number of numerical studies utilizing cosmological simulations focus on the detailed transition between these two regimes (e.g. Ocvirk, Pichon & Teyssier 2008; Brooks et al. 2009; Kereš & Hernquist 2009; Oppenheimer et al. 2010; Faucher-Giguère, Kereš & Ma 2011; van de Voort et al. 2011; Nelson et al. 2013), and how galactic feedback from stars or AGN and hydrodynamic instabilities affect this transition (e.g. Kereš & Hernquist 2009; Faucher-Giguere et al. 2015, 2016; Fielding et al. 2017; Nelson et al. 2019; Esmerian et al. 2020; Stern et al. 2020).

In the meantime, a significant observational effort has been devoted to disentangling the cold- and hot-mode accretion scenarios. For very large halo masses corresponding to galaxy clusters ($\gtrsim 10^{14}\,{\rm M}_\odot$), the

★ E-mail: suoqing@caltech.edu

virial temperature reaches $\gtrsim 10^7$ K that corresponds to a cooling time which is longer than the Hubble time. Hence, hot gaseous haloes are expected, and these have been observed in X-ray emission (Li et al. 2008; Anderson & Bregman 2011; Fang, Bullock & Boylan-Kolchin 2012) and Sunyaev–Zel'dovich (SZ) effect (Planck Collaboration XI 2013; Anderson, Churazov & Bregman 2015). On the other hand, evidence of cold-mode accretion, expected to predominate in much lower mass haloes, is relatively sparse due in great part to both low emissivities of cool halo gas (Faucher-Giguère et al. 2010; van de Voort & Schaye 2013; Sravan et al. 2016) and low covering fractions of Lyman limit systems that trace cold accretion streams and thus are hard to probe via absorption (Faucher-Giguère & Kereš 2011; Fumagalli et al. 2011; Faucher-Giguere et al. 2015; Hafen et al. 2017). Observational evidences have been significantly enriched by recent observations of circumgalactic medium (CGM; Tumlinson, Peeples & Werk 2017). At high redshifts, detected Ly α emission (Cantalupo et al. 2014; Hennawi et al. 2015; Martin et al. 2015; Cai et al. 2017) might suggest the existence of cold filamentary inflows (Dijkstra & Loeb 2009) or thermally radiating cool gas (Fardal et al. 2001). At low redshifts, observations via quasar absorption lines (Stocke et al. 2013; Werk et al. 2014; Stern et al. 2016; Prochaska et al. 2017) agree on a total mass of $\gtrsim 10^{10}$ M$_\odot$ of cool gas at $\sim 10^4$ K in MW-mass haloes, though whether the associated observations of high ionization lines (O VI , Ne VIII) indicate the existence of a virial shock is unclear (Stern et al. 2018; Burchett et al. 2019). Therefore, it becomes particularly interesting to ask whether virial shocks can form in those systems, and how the thermal state of halo gas is affected by the presence or absence of virial shocks.

In recent years, the impact of non-thermal processes on the halo gas, such as magnetic fields (e.g. Ji, Oh & McCourt 2018; van de Voort et al. 2020) and cosmic rays (CRs; e.g. Salem, Bryan & Corlies 2016; Farber et al. 2018; Ji et al. 2020; Buck et al. 2020; Butsky et al. 2020), is under increasingly active investigation. Ji et al. (2020) utilized FIRE-2 simulations[1] with CR physics incorporated (Chan et al. 2019; Hopkins et al. 2020c) to investigate the effects of CRs on the CGM properties. Hopkins et al. (2020c) and Ji et al. (2020) demonstrated that for certain assumptions about CR propagation, the CGM in MW-mass galaxy haloes can be supported by CR pressure rather than thermal pressure, which leads to dramatic changes of the physical states of halo gas. Ji et al. (2020) found that in non-CR haloes of MW mass ($\sim 10^{12}$ M$_\odot$), halo gas is primarily warm-hot ($\gtrsim 10^5$ K) with highly anisotropic, thermal pressure-confined cool filaments embedded, while in CR pressure-dominated ones, halo gas is much cooler at a few 10^4 K, and the CR pressure-supported cool phase is diffuse and volume-filling over the entire haloes. The gas kinematics in CR-dominated haloes are further discussed in Hopkins et al. (2020a) with an emphasis on outflows. This work will primarily focus on the impact of CRs on the properties of inflows, as well as its consequence for the formation of virial shocks and the thermal state of halo gas.

The outline of the paper is as follows. In Section 2, we describe our computational methods. In Section 3, we describe theoretical expectations, and in Section 4, we present our findings. We conclude in Section 5.

2 METHODS

The specific simulations studied here are the same as those presented and studied in Hopkins et al. (2020c) and Ji et al. (2020), where the details of the numerical methods are described. We therefore only briefly summarize here. The simulations were run with the GIZMO code[2] (Hopkins 2015), which solves the equations of idealized magnetohydrodynamics (MHD; Hopkins 2016; Hopkins & Raives 2016) incorporated with gravity, anisotropic Spitzer–Braginskii conduction and viscosity (Hopkins 2017; Su et al. 2017; Hopkins et al. 2020c). We also include the physics of gas cooling and heating, star formation, and stellar feedback from the FIRE-2 version of the Feedback in Realistic Environments (FIRE) project (Hopkins et al. 2014; Hopkins et al. 2018) with the meta-galactic background with the FG09 UVB model from Faucher-Giguere et al. (2009).

Our 'baseline' or 'MHD+' simulations include all the physics above except for CRs. Compared with the 'MHD+' simulations, our 'CR+' simulations incorporate additional CR physics described in details in Chan et al. (2019) and Hopkins et al. (2020c). We evolve 'single-bin' CRs at the energy of ∼GeV as an ultra-relativistic fluid with anisotropic streaming and diffusion (McKenzie & Voelk 1982), accounting for streaming and collisional losses (Guo & Oh 2008). CRs are sourced from the SNe ejecta kinetic energy, with a fixed fraction of $\epsilon_{\rm cr} = 0.1$ of SNe energy converted into CRs energy. To solve the CR transport equations, we adopt a two-moment method which is described in Chan et al. (2019) (similar to the scheme in Jiang & Oh 2018). We use a constant parallel diffusion coefficient $\kappa_\parallel = 3 \times 10^{29}\,{\rm cm^2\,s^{-1}}$ and a streaming speed $v_{\rm stream} = 3 v_{\rm A}$, where $v_{\rm A}$ is the local Alfvén speed.[3] The choice of the diffusion coefficient is calibrated by the observational constraints from e.g. spallation and more detailed measurements in the MW and gamma-ray emission in local galaxies (Hopkins et al. 2020c).

3 THEORETICAL EXPECTATIONS

Assume that we have a spherically symmetric, steady-state inflow from $r \to \infty$ into the center of a halo at $r \to 0$, in a halo which is approximately quasi-hydrostatic over a time-scale of ∼Gyr at low redshifts. The continuity equation in steady state ($\partial\rho/\partial t = 0$) requires $4\pi\,\rho\,r^2\,v_r = \dot{M}_{\rm in} = $constant as a function of radius, so we can replace $v_r \to \dot{M}_{\rm in}/4\pi\,\rho\,r^2$. The momentum equation, $r^{-2}\,\partial(\rho\,r^2\,v_r^2)/\partial r = -\partial P/\partial r + \rho\,\partial\Phi/\partial r$, can then be written as

$$\left(\frac{\dot{M}_{\rm in}}{4\pi\,\rho\,r^2}\right)^2 \left(2 + \frac{{\rm d}\ln\rho}{{\rm d}\ln r}\right) + \frac{1}{\rho}\,\frac{{\rm d}P}{{\rm d}\ln r} + V_c^2(r) = 0. \quad (1)$$

3.1 Without CRs

The case without CRs where the gas is in hydrostatic equilibrium in a halo is extensively studied in the literature, and we will only briefly mention it here for reference.

Without CRs, assume the pressure is primarily gas thermal pressure. First, consider a simple case where the gas should follow a single adiabat, i.e. $P \propto \rho^\gamma$. At large radii when gas is falling in from the cosmic web (before a shock), the gas is approximately isothermal at the temperature set by photoionization equilibrium, so $P \approx \rho\,c_s^2$, which allows us to write equation (1) as $(\partial\ln\tilde{\rho}/\partial\ln r)\,(1 + \tilde{\rho}^{-2}) = 2 - (V_c/c_s)^2$ with $\tilde{\rho} \equiv 4\pi\,c_s\,r^2\,\rho/\dot{M}_{\rm in}$ and circular velocity $V_c(r) = \sqrt{GM(r)/r}$. When $V_c \gtrsim \sqrt{2}\,c_s$ (all cases of interest here), for any reasonable potential profile (e.g. Hernquist 1990; Navarro,

[1] http://fire.northwestern.edu

[2] A public version of GIZMO is available at http://www.tapir.caltech.edu/~phopkins/Site/GIZMO.html

[3] However, the streaming heating term is still calculated with $v_{\rm A}$, not $v_{\rm stream}$. We have also explicitly checked that setting $v_{\rm stream} = v_{\rm A}$ does not cause any significant differences for the distribution of halo gas.

Frenk & White 1996 profiles), it is easy to verify that this equation has no physical, smooth solutions that continuously connect $r \rightarrow 0$ to $r \rightarrow \infty$. Furthermore, it is easy to extend this to any adiabat $P \approx P_0\,(\rho/\rho_0)^{\gamma}$ and show the same for $V_c \gg c_s$. For a form of V_c which generically transitions from flat or rising at small r to falling at large r, the solutions for ρ and P tend to diverge around this critical radius (i.e. $\sim R_{\rm vir}$).

This simply indicates that the gas must undergo some sort of shock or change in entropy as it flows in; as is well known, this does not necessarily imply a 'standing' virial shock. As a rule, although shocks occur as the gas flows in whenever the maximum halo circular velocity $V_{\rm max} \gg 10\,{\rm km\,s^{-1}}$ (the isothermal temperature of the IGM), if the post-shock cooling time $t_{\rm cool}$ is much less than the dynamical time $t_{\rm dyn}$ at the shock radius ($\sim R_{\rm vir}$, giving $t_{\rm dyn} \sim 0.1\,t_{\rm Hubble}$), the gas essentially free-falls on to the galaxy in a 'cold flow' and no stable, standing shock forms. On the other hand in haloes with $M_{\rm halo} \gtrsim 10^{11}\,{\rm M_\odot}$, $t_{\rm cool} \gtrsim t_{\rm dyn}$ and a virial shock tends to form covering most of the solid angle around the halo, even if a significant fraction of the gas actually accreted by the galaxy comes in via filaments that can 'punch through' this hot halo.

3.2 In CR-dominated haloes

The case of particular interest is where CR pressure *dominates* over thermal pressure in the CGM. A simple analytic model for this regime is discussed in more detail in Hopkins et al. (2020c), as well as Ji et al. (2020) and Hopkins et al. (2020a), so we only briefly review here. For a constant effective (angle-averaged) diffusivity $\tilde{\kappa}$ which is large enough ($\tilde{\kappa} \gtrsim 10^{29}\,{\rm cm^2\,s^{-1}}$) and galaxy central gas densities which are low enough (e.g. like MW and lower mass 'normal' galaxies at $z \sim 0$, but much lower than observed starburst systems such as M82 or Arp220), the CRs escape and form a quasi-equilibrium, diffusion-dominated steady-state energy–density profile with $P_{\rm cr} \approx \dot{E}_{\rm cr}/(12\pi\,\tilde{\kappa}\,r)$ at $r < r_{\rm stream}$ and $P_{\rm cr} \approx \dot{E}_{\rm cr}/(12\pi\,v_{\rm stream}\,r^2)$ at $r > r_{\rm stream}$, with $r_{\rm stream} \equiv \tilde{\kappa}/v_{\rm stream} \sim \tilde{\kappa}/v_A(r_{\rm stream})$. Here, $\dot{E}_{\rm cr} = \epsilon_{\rm cr}\,\dot{E}_{\rm SNe} = \epsilon_{\rm cr}\,u_{\rm SNe}\,\dot{M}_*$ is the CR injection rate. If the above conditions are met, this can dominate over gas thermal pressure and be the dominant source of pressure support for gas from radii outside the disc to $>R_{\rm vir}$, in haloes which are sufficiently massive ($\gtrsim 10^{11}\,{\rm M_\odot}$, where SFR and therefore $\dot{E}_{\rm cr}$ is sufficiently large), star forming and low redshift ($z \lesssim 1-2$, where densities are low enough for CRs to escape and the gas densities are sufficiently low for CR pressure to dominate).

So let us assume $P \approx P_{\rm cr} \approx \dot{E}_{\rm cr}/(12\pi\,\tilde{\kappa}\,r\,[1 + r/r_{\rm stream}])$ dominates the pressure. As discussed in the papers above, this immediately defines a critical equilibrium density profile $\rho_{\rm eq}$ where ${\rm d}P/{\rm d}r = \rho_{\rm eq} V_c^2/r$, i.e. where CR pressure balances gravity: denser gas ($\rho > \rho_{\rm eq}$) will sink, while less dense gas ($\rho < \rho_{\rm eq}$) will be accelerated outwards. Because the injection rate $\dot{E}_{\rm cr}$ is time-averaged over the CR diffusion time out to r ($\gtrsim$ Gyr at the radii of interest), it is not sensitive to short-time-scale fluctuations in SFR. Moreover, because the CRs diffuse rapidly on small scales through any structure, this profile is essentially independent of perturbations to the local inflow rate and gas density structure. Inserting this in equation (1), it is easy to integrate numerically and verify (for any reasonable $V_c(r)$ profile) not only that there are trivial solutions with constant inflow $\dot{M}_{\rm in}$, but that these solutions are *smooth*, continuous, infinitely differentiable, positive-definite, and monotonic in ρ and v_r.

If we assume the potential follows a Hernquist (1990) or Navarro et al. (1996) profile, then at small r, $V_c^2 \propto r/r_s$ (where r_s is a halo scale length). If we also take $r \ll r_{\rm stream}$, then the solutions become $\rho \rightarrow \rho_{\rm eq} = \dot{E}_{\rm cr}/(12\pi\,\tilde{\kappa}\,r\,V_c^2(r)) \propto r^{-2}$, with $v_r \rightarrow (3\,\dot{M}_{\rm in}\,\tilde{\kappa}/\dot{E}_{\rm cr})\,(V_c^2/r) \approx$ constant [so the inflow rate can be written as $\dot{M}_{\rm in} = (\dot{E}_{\rm cr}\,v_r/3\,\tilde{\kappa})\,(r/V_c^2)$]. Inserting $\epsilon_{\rm cr} = 0.1$, the value of $u_{\rm SNe}$ for our adopted IMF, $\tilde{\kappa}_{29} \equiv \tilde{\kappa}/10^{29}\,{\rm cm^2\,s^{-1}}$, and the standard virial scalings for dark matter haloes for r_s and $V_c(<r_s)$, this gives $\dot{M}_{\rm in}/\dot{M}_* \sim 0.6\,(1+z)^{-2}\,(v_r/10\,{\rm km\,s^{-1}})\,(\Delta\Omega/4\pi)\,\tilde{\kappa}_{29}^{-1}\,(M_{\rm halo}/10^{12}\,{\rm M_\odot})^{-1/3}$, where $\Delta\Omega$ is the solid angle covered by the inflow (assuming constant-$\Delta\Omega$). At large radii ($r \gg r_s,\ r_{\rm stream}$), if we assume $V_c^2 \propto r^{-1}$ (e.g. a Keplerian or Hernquist 1990 profile), then ρ and v_r both gradually decline $\propto 1/r$ (our derivation does not include the Hubble flow at large r, so this is the 'correct' behaviour).

In short, CR-dominated solutions *allow* for smooth quasi-isothermal inflow of gas from infinity into the halo, *without a virial shock*. These solutions have $\rho \propto v_r \propto r^{-1}$ at large radii and $\rho \propto r^{-2}$, $v_r \sim v_{\rm terminal} \sim$ constant at small radii, without a discontinuity in the gas properties. They feature inflow rates comparable to or larger than galaxy SFRs for relatively modest (transonic or mildly supersonic) inflow velocities.[4]

4 RESULTS

We begin by focusing on a representative case study of one MW-like, $10^{12}\,{\rm M_\odot}$ halo (m12i) from our suite. In Hopkins et al. (2020c) and Ji et al. (2020), we show that at $z = 0$, the CR+ run of m12i studied here has CR pressure much larger than thermal pressure in CGM gas at radii $\lesssim$500 kpc, making this an excellent example of a 'CR pressure-dominated halo'. In Section 4.6, we examine additional haloes to explore mass and environmental dependencies.

4.1 Spatial structure

Fig. 1 shows slice plots (edge-on to the disc) taken from the snapshot at $z = 0$ from the MHD+ and CR+ runs of m12i halo. In the top panel, MHD+ unambiguously produces a hot halo at $T \gtrsim 10^6$ K, with virial shock fronts at $r \sim 300$ kpc indicated by temperature jumps. However, such a hot halo is absent from CR+; instead, a low-temperature 'void' at $T \sim$ a few 10^4 K forms roughly aligned with bipolar directions, surrounded by warm ambient medium of $\sim 10^5$ K around $r \sim 200$ kpc.

The velocity structure is shown in the middle panel of Fig. 1, where the velocity streamlines are plotted in black lines and the background colour represents the magnitude of the radial velocity v_r, with white contours at values of $v_r = 0$. MHD+ shows inflow in all directions from the cosmic web on to a clear and large-scale coherent ($\gtrsim$100 kpc) virial shock at $r \sim 300$ kpc, with a turbulent, inflow-dominated halo interior to this. In contrast, CR+ shows inflow penetrating the mid-plane down to $r \sim 100$ kpc and strong bipolar outflow extending beyond 500 kpc, with no apparent virial shock. It is worth noting that by comparing the velocity and temperature plots, we can see that in CR+, the mid-plane inflow appears co-spatial with the warm (10^5 K) region, and the bipolar outflow corresponds to the cool (a few 10^4 K) gas. Detailed analysis on inflow/outflow properties will be discussed later in Section 4.2.

The shock structure can be observed clearly by plotting the negative of the velocity divergence $-\nabla\cdot\boldsymbol{v}$, as shown in the bottom panel in Fig. 1, where large positive values indicate converging flow at shock fronts. For MHD+, inflowing streams are weakly compressed

[4]It is also worth pointing out that the infall rate and SFR are not independent of each other. Instead, the infall rate is required to be least equal to SFR, or higher to account for outflows.

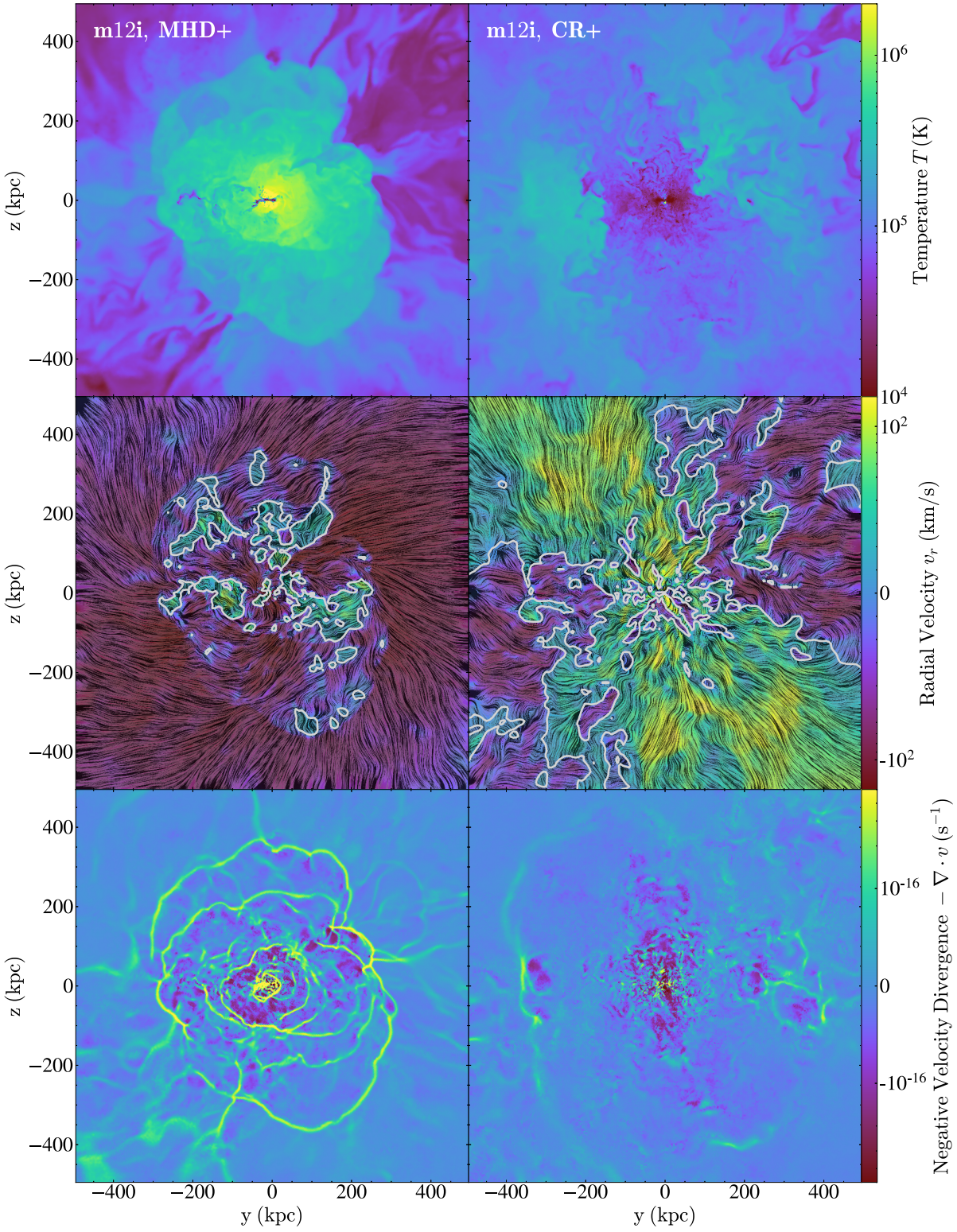

Figure 1. Slice plots edge-on to the disc of (top) gas temperatures, (*middle*) radial velocities superimposed with black velocity streamlines and white contours at $v_r = 0$), and (*bottom*) negative velocity divergences, in 'MHD+' (*left*) and 'CR+' (*right*) runs for m12i halo at $z = 0$. MHD+ features a hot halo with clear shock fronts peaking $-\nabla \cdot \boldsymbol{v}$, with the CGM dominated by inflows and trapped outflows. In the CR+ run, we see a much cooler halo, with extended outflows and much less apparent shocks except for mild compression at $r \sim R_{\rm vir}$.

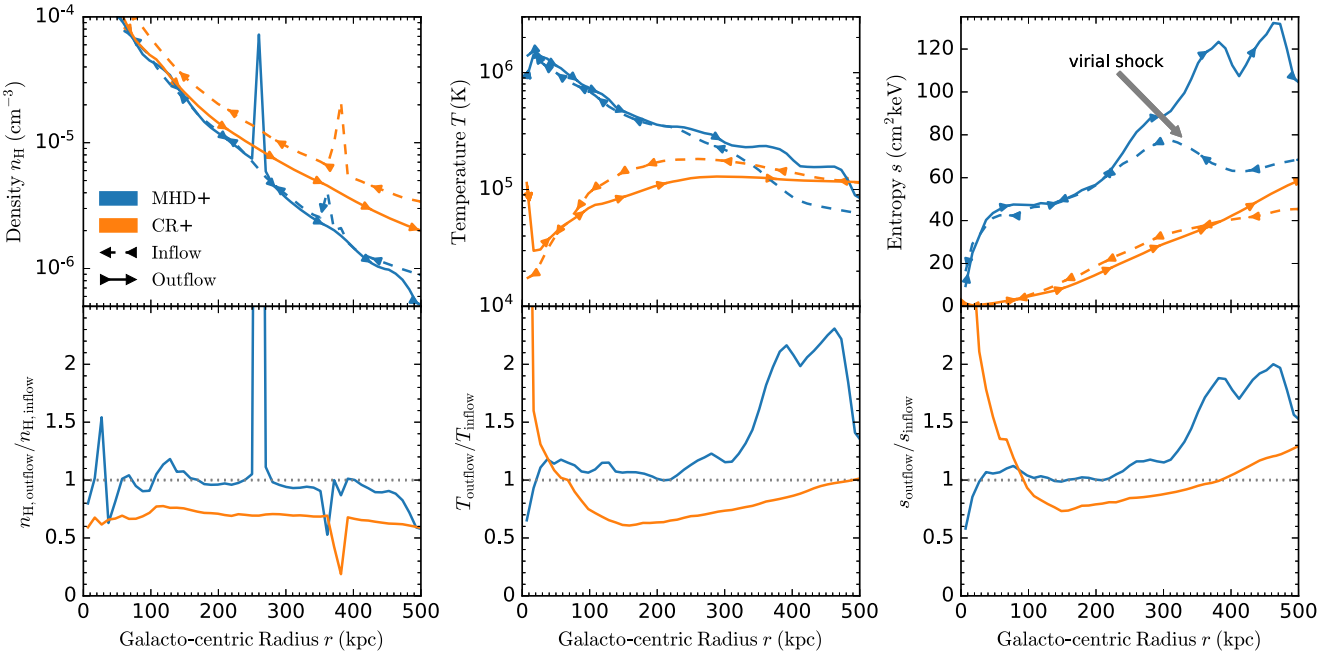

Figure 2. Top: volume-averaged radial profiles of gas number density (*left*), temperature (*middle*) and entropy (*right*) of inflows (*dashed with leftward arrows*) and outflows (*solid with rightward arrows*) for the MHD+ (*blue*) and CR+ (*orange*) runs of the m12i halo at $z = 0$. Bottom panels show the ratios of the inflow and outflow values. Plotted values are volume-averaged in spherical shells at galacto-centric radius r. In MHD+, outflows have higher temperature and entropy than inflows beyond the virial shock ($r \gtrsim 300$ kpc), while inside the virial shock ($r \lesssim 300$ kpc) the density, temperature, and entropy of inflows and outflows are similar. In CR+, the density, temperature, and entropy of outflows are lower than inflows at most radii by a factor of a couple; the temperature and entropy of both inflows and outflows are lower as well. Note the 'spikes' in n_H at certain r owe to the exact location of a satellite galaxy in this snapshot.

until they reach $r \sim 300$ kpc where the first shock front forms and encloses the entire halo. Inside the shock-enclosed halo, a series of additional shocks are triggered at $r < 300$ kpc by the interaction between inflows and outflows. In contrast, for CR+, no spatially coherent shock structure is observed, and the gas is only mildly compressed within limited regions around $r \sim 400$ kpc. Within $r \sim 100$ kpc in CR+, relatively large fluctuations in $\nabla \cdot \boldsymbol{v}$ appear due to supersonic turbulence, as discussed later in Section 4.2.2.

In short, a prominent, solid-angle covering virial shock is absent from CR-dominated haloes; the halo gas is cooler at a few 10^4 K with extended bipolar outflows. In contrast, shocks are prevalent in non-CR haloes around and within the virial radius which heats up the halo gas to the virial temperature; the halo is inflow-dominated, and outflows are sparse and trapped inside the virial radius (the latter point is discussed in details in Hopkins et al. 2020a). Compared to the MHD+ case, the CR+ run shows highly anisotropic spatial structures (Qu & Bregman 2019).

4.2 Properties of inflows and outflows

To probe the shock structure quantitatively, Fig. 2 presents the density, temperature and entropy profiles respectively for inflows and outflows in the MHD+ and CR+ runs. Fig. 3 shows the inflow/outflow radial velocities, mass fluxes and turbulent velocities.

4.2.1 Outflows

Hopkins et al. (2020a) present a detailed study of the effect of CRs on outflows in these simulations, so we only briefly summarize outflows here (as they are relevant for some inflow behaviours). In MHD+, outflows are quasi-spherical; they have similar density compared to inflows but higher temperature/entropy/thermal pressure (especially outside $\sim R_{vir}$); and the outflow temperature, radial velocity, and mass flux all decline with increasing radius r. Outflow velocities are also subsonic and subvirial, and the outflows appear well mixed with inflows well inside of R_{vir}. All of these are generic properties expected of trapped thermal-pressure-driven outflows.

In CR+, outflows are bipolar and are not well mixed with inflows: the outflow velocity v_r and mass flux $\dot{M}_{out}$ are approximately constant with radius (not trapped), with $\dot{M}_{out} \sim 2\,\dot{M}_*\,(v_r/30\,\mathrm{km\,s^{-1}})$ in good agreement with the analytic CR-pressure-dominated inflow solutions from Section 3 (given the values $\tilde{\kappa}_{29} \sim 1$, $M_{halo} \sim 10^{12}\,M_\odot$, $z \sim 0$, $\Delta\Omega/4\pi \sim 1/2$ appropriate for this snapshot). Outflows are approximately isothermal and have lower temperature/entropy/thermal pressure compared to inflows, indicating they are driven by non-thermal (CR) pressure. Finally in CR+, outflows have lower densities, higher velocities, and similar mass fluxes compared to inflows: all of these can again be predicted from our simple analytic model (see Section 3): gas with $\rho < \rho_{eq}$ is accelerated outward by CR pressure while gas with $\rho > \rho_{eq}$ sinks (since gravity exceeds CR pressure forces), so $\rho_{outflow} < \rho_{eq} < \rho_{inflow}$ should be true at all r (and indeed we find $\langle\rho_{outflow}\rangle/\langle\rho_{inflow}\rangle \sim 0.6$ at all r). Moreover, as shown in Hopkins et al. (2020a), a parcel of gas with some initial density $\rho_i \neq \rho_{eq}$ (so CR and gravity forces are imbalanced) is accelerated to a terminal speed $|v_r| \propto (\rho_i/\rho_{eq}[r_i])^{-1/2}$: so we should expect $v_{outflow}/v_{inflow} \sim (\rho_{outflow}/\rho_{inflow})^{-1/2} \sim 1.3 > 1$. Using $\dot{M} \propto \rho\, v_r$, we then have $|\dot{M}_{outflow}|/|\dot{M}_{inflow}| \propto (\rho_{outflow}/\rho_{inflow})^{1/2} \sim 0.8 < 1$.

4.2.2 Inflows

In MHD+, beginning from $r > 500$ kpc, inflows gradually accelerate to larger $|v_r|$ as they fall to smaller r (Fig. 3), maintaining the

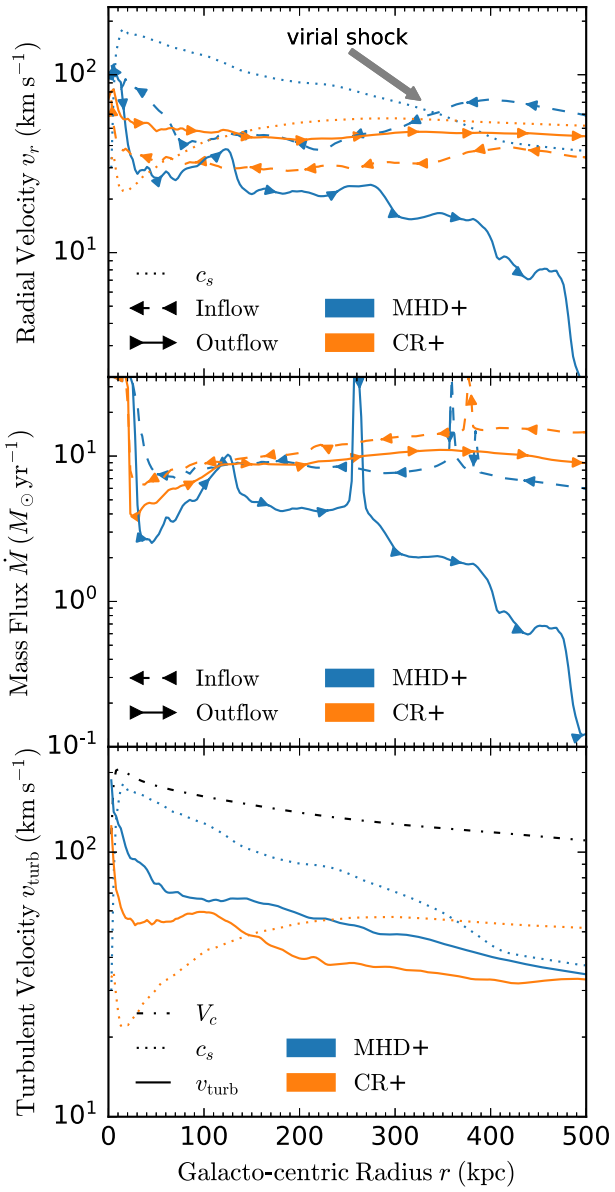

Figure 3. Radial profiles of radial velocities (*top*), and mass fluxes (*middle*) and turbulent velocities (*bottom*) of inflows (*dashed with leftward arrows*) and outflows (*solid with rightward arrows*) for the MHD+ (*blue*) and CR+ (*orange*) runs of the m12i halo at $z = 0$ (as Fig. 2). Thermal sound speeds c_s (dotted) and circular velocities V_c (dash-dotted) are also shown for reference. MHD+ is dominated by inflows while the outflows are hot (Fig. 2) but slow and $\dot{M}$, v_r drop rapid with r, indicating trapping. In CR+, both inflows and outflows have roughly constant fluxes and velocities with radius (i.e. are not trapped or decelerated); outflows are faster, but inflows carry slightly larger mass flux. The $\dot{M}_{\rm in}$ profile is quite consistent with the CR-dominant $\dot{M}$ solutions discussed in Section 3.2; requiring $\dot{M}_{\rm in} \sim \dot{M}_{\rm out} + \dot{M}_*$ further gives $\dot{M}_{\rm out} \sim \frac{1}{2}\dot{M}_{\rm in}$, as shown in the middle panel. Note the 'spikes' in $\dot{M}$ at certain r owe to the exact location of a satellite galaxy in this snapshot. Turbulence is subsonic in MHD+ and at large radii ($r \gtrsim 100$ kpc) in CR+, but transits to supersonic in the inner halo ($r \lesssim 100$ kpc) of CR+ due to the decrease of the sound speed towards smaller radii, as shown in the bottom panel. Here, we estimate turbulent velocities by computing velocity dispersions of v_θ and v_ϕ while excluding v_r in spherical coordinates, since δv_r is dominated by the shear motion between coherent inflows outflows which is actually not turbulence.

approximately isothermal IGM temperature (slightly decreasing their entropy as ρ increases; Fig. 2), until they suddenly de-celerate and increase in temperature and entropy at $r \sim 300$ kpc $\sim R_{\rm vir}$ (the clear position of the virial shock in Fig. 1). Inside of $R_{\rm vir}$, $\dot{M}_{\rm in}$ remains approximately constant, with inflows and outflows at similar ρ, T, s (the result of efficient inflow/outflow mixing), with densities and temperatures increasing and entropies decreasing at small r and subsonic v_r, indicative of a classic quasi-hydrostatic cooling-flow (i.e. 'hot halo') solution (see e.g. Stern et al. 2020), for more discussion of these solutions in our non-CR runs).

The CR+ run, in contrast, does not exhibit these signatures. The inflow velocity $v_r \sim 30 - 40\,{\rm km\,s^{-1}}$ and temperature $T \sim 10^5$ K remain approximately constant from $r \gtrsim 500$ kpc to $r \ll 100$ kpc, while entropy s gradually declines as n gradually rises at smaller r. As detailed above, the inflowing gas is systematically more dense and slower than outflows (with slightly higher $\dot{M}$), as expected from analytic steady-state models of gas in a CR-pressure-dominated halo. As the gas is cooler, inflow velocities are trans-sonic at most radii. As discussed in Ji et al. (2020), gas densities of both inflows and outflows are higher, especially at large r, compared to the MHD+ run, as the additional CR pressure can simply support more gas against gravity. Given the $z \sim 0$ SFR of this galaxy $\dot{M}_* \sim 2$–$3\,{\rm M_\odot\,yr^{-1}}$ and v_r, the inflow rate $\dot{M}_{\rm inflow}$ agrees remarkably well with our order-of-magnitude scaling for a steady-state CR-pressure dominated inflow in Section 3.

In the left-hand panel of Fig. 2, the overall gas density in CR+ is higher than that in MHD+ by a factor of a few, and notably, the density outflow-to-inflow ratios in MHD+ and CR+ differs distinctly: in MHD+, the inflow and outflow densities are similar, but in CR+, the density of outflows is systematically lower than inflows with the ratio $n_{\rm H,outflow}/n_{\rm H,inflow} \sim 0.6$–$0.7 < 1$, which holds for a wide special range over 500 kpc. This is consistent with previous findings in Ji et al. (2020) and our theoretical expectations: gas with $\rho < \rho_{\rm eq}$ is accelerated outward by CR pressure gradients, while gas with $\rho > \rho_{\rm eq}$ falls towards the galactic centre since gravity exceeds CR pressure support locally, therefore the order $\rho_{\rm outflow} < \rho_{\rm eq} < \rho_{\rm inflow}$ is always valid.

The middle panel of Fig. 2 shows temperature profiles. In MHD+, the temperatures of both inflows and outflows increase with de-creasing radius; outflows are warmer than inflows by a factor of 2 at large radii of $r \gtrsim 300$ kpc. At smaller radii of $r \lesssim 300$ kpc, the temperatures of inflows and outflows are similar. This is consistent with the virial shock picture in non-CR haloes: cooler inflows hit on to the virial shock front at $r \sim 300$ kpc, get heated up by dumping shock kinetic energy into thermal energy, and become fully mixed into highly turbulent gas inside the virial shock where the inflows and outflows have the same temperature. Such an apparent signature of shocks is absent from the CR+ run: both inflows and outflows are nearly isothermal at $T \sim 10^5$ K for $r \gtrsim 150$ kpc; outflows are cooler than inflows at most radii, in contrast to MHD+ where outflows are hotter at large radii. The difference in temperatures between inflows and outflows suggests the mixing of inflows and outflows is inefficient in CR+, which can also be seen from Fig. 1 as well, where inflows and bi-conical outflows trace different paths with clear boundaries between each other without significant mixing.

In the right-hand panel of Fig. 2, the entropy of inflows in MHD+ shows a bulge at $r \sim 300$ kpc due to virial shock heating, and the entropy of outflows is ~2 times higher than inflows at large radii. At $r \lesssim 200$, kpc, inflows and outflows have the same entropy, indicating efficient mixing within shocked haloes. In CR+, the entropy of both inflows and outflows monotonically and smoothly decrease towards smaller radii, without shock-induced entropy input. Inside CR-

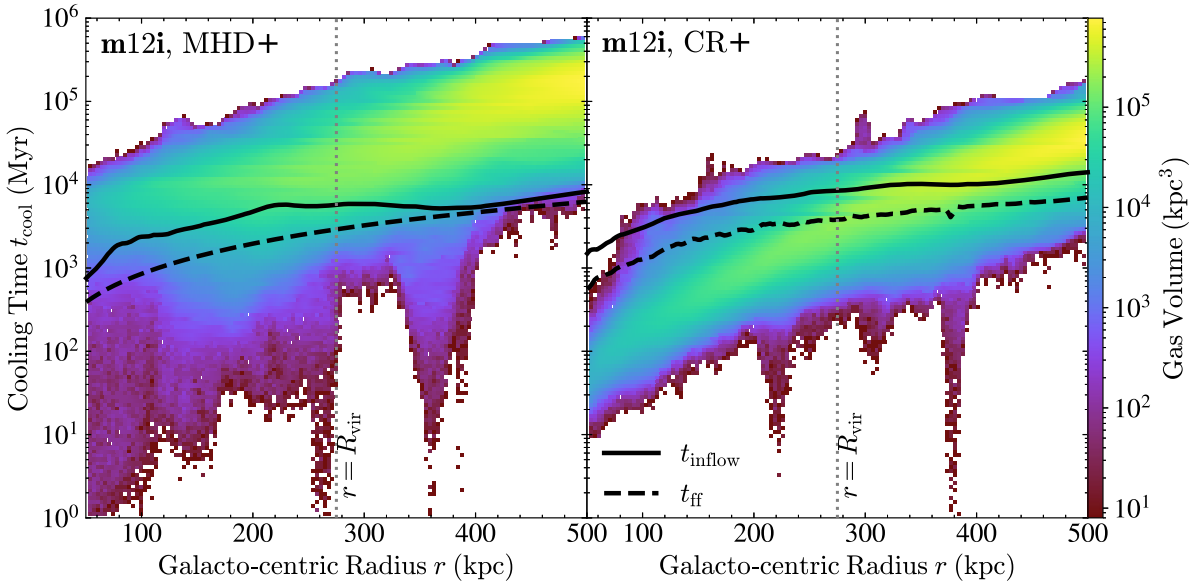

Figure 4. Radial profiles of cooling time $t_{\rm cool} = 3/2\,kT/n\Lambda$ (*colour*) weighted by gas volume, superposed with profiles of inflow time $t_{\rm inflow} = r/v_{\rm inflow}$ (*solid*) and effective free-all time $t_{\rm ff} = \sqrt{2r/(\nabla\Phi + \nabla P_{\rm cr}/\rho)}$ (*dashed*) in the MHD+ (*blue*) and CR+ (*orange*) runs of the m12i halo at $z = 0$, where the location of $R_{\rm vir}$ marked with a dotted vertical line. The cooling time of the volume-filling phase in MHD+ is longer than CR+ by one order of magnitude or more. Compared to MHD+, CR pressure support in the CR+ run slightly increases $t_{\rm ff}$ and $t_{\rm inflow}$, but the large temperature difference (Fig. 2) leads to much lower T and hence $t_{\rm cool}$ in CR+, making $t_{\rm cool} \lesssim t_{\rm inflow}$, $t_{\rm ff}$ for $r \lesssim 300$–400 kpc in CR+ (while $t_{\rm cool} \gtrsim t_{\rm inflow}$ within $R_{\rm vir}$ and $t_{\rm cool} \gg t_{\rm inflow}$, $t_{\rm ff}$ outside $R_{\rm vir}$ in MHD+).

dominated haloes at $100\,{\rm kpc} \lesssim r \lesssim 400\,{\rm kpc}$, outflows carry lower entropy than inflows.

After examining the fluid properties of inflows and outflows respectively in both MHD+ and CR+, we find that CRs dramatically change gas dynamics in galaxy haloes as well as the existence of virial shocks. In non-CR haloes, cool gas carrying low entropy flows inwards until it hits on to the virial shock front at $r \sim 300$ kpc, where it meets hot, high-entropy outflowing gas and is heated by shock kinetic energy dissipation. Cool inflows and hot outflows are fully mixed with each other and reach the same temperature and entropy inside the virial shock front; there is no significant difference in gas densities between outflows and inflows in non-CR haloes. However, CR-dominated haloes behave in an opposite way by featuring cooler, lower-density and lower-entropy outflows along bi-polar directions compared with inflows. Consequently, in CR-dominated haloes, inflows and outflows are not in thermal pressure equilibrium; instead, outflows are under-pressured relative to inflows with $P_{\rm thermal,outflow} < P_{\rm thermal,inflow}$, but still in total pressure equilibrium with CR pressure taken into account, i.e. $P_{\rm thermal}(r) + P_{\rm cr}(r) \approx$ constant at a given r (Ji et al. 2020). This suggests that CRs are more abundant in bi-conical outflow regions than inflow regions.

As previously discussed, in CR-dominated haloes, gas with density ρ_i deviating from $\rho_{\rm eq}$ feels an imbalance between CR pressure gradients and gravity, and thus is subject to local acceleration. Such a parcel of gas with density ρ_i is accelerated to a terminal speed of $v_r \propto (\rho_i/\rho_{\rm eq})^{-1/2}$ (Hopkins et al. 2020a). Then given $\rho_{\rm outflow}/\rho_{\rm inflow} \sim 0.6$–$0.7$ observed in Fig. 2, we have $|v_{\rm outflow}|/|v_{\rm inflow}| \propto (\rho_{\rm outflow}/\rho_{\rm inflow})^{-1/2} > 1$, and mass flux $|\dot{M}_{\rm outflow}|/|\dot{M}_{\rm inflow}| \propto (\rho_{\rm outflow}/\rho_{\rm inflow})^{1/2} < 1$, where $\dot{M} \propto \rho v_r$. These ratios turn out to be consistent with profiles plotted in Fig. 3, where for CR+ (orange lines), radial velocity (top panel) is outflow-dominated, while mass flux (middle panel) is inflow dominated. And for MHD+ (blue lines in Fig. 3), both radial velocity and mass flux are dominated by inflows; radial velocity and mass flux associated with outflows rapidly decline with radius, indicating outflows are significantly trapped. In addition, due to the decrease of temperature at small radii of $r \lesssim 100$ kpc in CR+ (middle panel of Fig. 2), the local sound speed drops below turbulent velocities and supersonic turbulence develops, as shown in the bottom panel of Fig. 3. The supersonic turbulence in the inner-halo region is reflected by relatively large $\nabla \cdot v$ fluctuations at small radii of the CR-dominated halo (the bottom panel of Fig. 1).

We notice that due to the presence of CR pressure gradients, a *much lower* inflow velocity in CR+ than in MHD+ even outside $R_{\rm vir}$ is predicted by our analytic model and demonstrated by our simulations, which leads to two consequences. First, the inflow velocity (orange dashed line in the top panel of Fig. 3) is already significantly *subsonic* at $r \gtrsim R_{\rm vir}$; therefore, a virial shock is not expected to develop, while in MHD+, inflows (blue dashed line in the top panel of Fig. 3) travel at a speed exceeding the sound speed and thus is *supersonic* outside $R_{\rm vir}$, until they hit on to virial shocks that raise local sound speed and become subsonic. Secondly, the inflow velocity in CR+ is reduced as if the gas is falling into a much lower potential, which effectively shifts the halo-mass scale to the level characteristic of $M_{\rm halo} \sim 10^{11}\,{\rm M}_\odot$, where gas would be heated to $\sim 2 \times 10^5$ K, if shocked. Therefore even if gas did shock, cooling at this temperature range would be too efficient to establish a stable atmosphere. We discuss the efficiency of gas cooling in more detail below.

4.3 Conditions for the formation of a stable virial shock

We discuss a sufficient condition that accounts for the absence of virial shocks in our CR+ run. Since CR heating in the CGM is negligible (Ji et al. 2020), the leading terms governing gas thermal energy $E_{\rm thermal}$ are adiabatic $P{\rm d}V$ work applied to gas and radiative cooling: ${\rm d}E_{\rm thermal}/{\rm d}t \sim P{\rm d}V/{\rm d}t - \int n^2 \Lambda {\rm d}V$, where ${\rm d}V$ is the volume element and Λ is the cooling coefficient. A viral shock cannot form if gas is net cooling, which in spherical symmetry we can write as ${\rm d}E_{\rm thermal}/{\rm d}t \sim 4\pi r^2 (P v_r - \int n^2 \Lambda {\rm d}r) \lesssim 0$. Defining the cooling time and inflow time as $t_{\rm cool} \equiv 3/2kT/n\Lambda$ and $t_{\rm inflow} \equiv r/v_r$, we can see this is

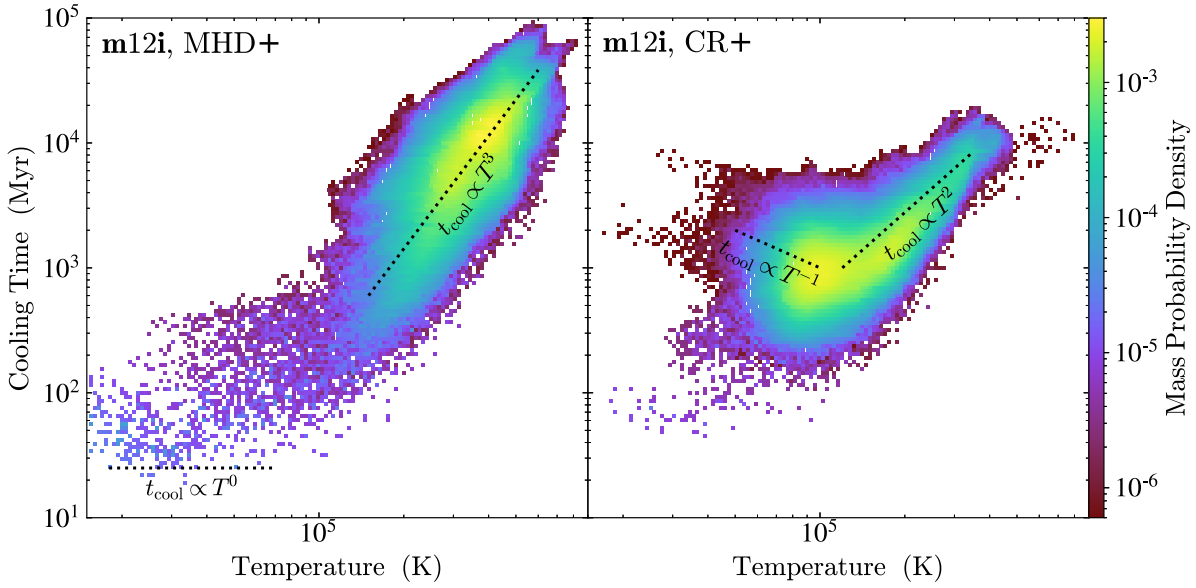

Figure 5. Temperature-cooling time-phase diagrams of gas in MHD+ (*left*) and CR+ (*right*) runs of m12i at $z = 0$ calculated with the real cooling curve. We show gas in a narrow spherical shell at radius $r \approx 200$ kpc; therefore, the gas pressure is approximately constant over the shell. For gas in warm and hot ($t \gtrsim 10^5$ K) phases, $t_{\rm cool}$ in CR+ follows a shallower power law, and thus is greater than MHD+ at a given T. For gas at a cooler phase ($T \lesssim 10^5$ K), $t_{\rm cool}$ in CR+ increases with decreasing temperatures, indicating that gas becomes harder to cool after reaching $\sim 10^5$ K when CR pressure is dominant. The difference of $t_{\rm cool}$ dependence on T between MHD+ and CR+ owes to the difference in temperature T where most of the gas resides, which is determined by thermal/CR pressure support – see more detailed discussions in the text.

equivalent to $t_{\rm cool} \lesssim t_{\rm inflow}$. When this condition is satisfied, inflowing gas can radiate away its thermal energy before accreting, and thus remain cool without creating a shock. We note that the definition of $t_{\rm cool}$ here does not include any heating terms, such as photon-heating, CR heating, turbulent heating or CR adiabatic heating/cooling, since $t_{\rm cool}$ is used to evaluate how quickly gas cools when the gas deviates from its equilibrium temperature which is co-determined by gas cooling and heating sources. We briefly discuss additional heating terms in more detail in Section 4.5.

Fig. 4 shows radial profiles of cooling time $t_{\rm cool}$ (coloured, weighted by gas volumes) and inflow time $t_{\rm inflow}$ (solid, weighted by gas volumes in inflow regions) in our m12i runs. Since CR pressure is decoupled from gas thermal pressure and resists infall, we define an effective free-fall time $t_{\rm ff} \equiv \sqrt{2r/(\nabla\Phi + \nabla P_{\rm cr}/\rho)}$ (with Φ the gravity potential) to include the effects of CRs. For MHD+, the relation $t_{\rm cool} \gtrsim t_{\rm inflow}$ always holds at outer CGM and IGM radii. However, in CR+, $t_{\rm cool} \ll t_{\rm inflow}$ at $r \lesssim 360$ kpc. From $t_{\rm ff}$ and $t_{\rm inflow}$, we see that CR pressure support in CR+ can mildly delay gas inflow, but this effect is order-unity. The dominant effect here is that $t_{\rm cool}$ in CR+ is an order of magnitude or more lower than in MHD+. For infalling gas (especially outside $R_{\rm vir}$), this owes to (1) higher gas densities supported by CR pressure (Fig. 2), (2) lower temperatures (more dominant inside $R_{\rm vir}$, owing to the lack of a shock), and (3) differences in the thermal phase structure within a given shell, discussed below.

4.4 Cooling efficiency with and without dominant CR pressure

To better understand why cooling is more efficient in CR+, we derive some scaling relations for $t_{\rm cool}$ as follows. Since thermal pressure equilibrium is satisfied in MHD+, at any fixed radius, $P \sim nk_{\rm B}T \sim$ constant locally (within a shell at a distance), therefore $n \propto T^{-1}$ (see Ji et al. 2020). With the definition of $t_{\rm cool}$ and the following very simple power-law approximation of the cooling function (sufficient for illustrative purposes here)

$$\Lambda(T) \propto \begin{cases} T & \text{for } T \lesssim 10^5\,\text{K} \\ T^{-1} & \text{for } T \gtrsim 10^5\,\text{K} \end{cases}, \tag{2}$$

the cooling time in MHD+ should roughly obey

$$t_{\rm cool,MHD} \propto \begin{cases} T^0 & \text{for } T \lesssim 10^5\,\text{K} \\ T^3 & \text{for } T \gtrsim 10^5\,\text{K} \end{cases}, \tag{3}$$

at a given radius r (Hollenbach & McKee 1979). In contrast, in CR+, since halo gas is supported by CR pressure rather than thermal pressure, the gas density profile $\rho \sim \rho_{\rm eq} = f(\dot{E}_{\rm cr}, \tilde{\kappa}, r, ...)$, where $\dot{E}_{\rm cr}$ and $\tilde{\kappa}$ are the CR luminosity and the CR effective diffusion coefficient (Ji et al. 2020), thus the gas density is independent of temperature, i.e. $\rho \propto T^0$. Therefore, we expect

$$t_{\rm cool,CR} \propto \begin{cases} T^{-1} & \text{for } T \lesssim 10^5\,\text{K} \\ T^2 & \text{for } T \gtrsim 10^5\,\text{K} \end{cases}, \tag{4}$$

at a given radius r.

We find that these toy relations for $t_{\rm cool}$ are consistent with our simulations, as shown in Fig. 5, where gas within a shell at $r \sim 200$ kpc is plotted on 2D phase diagrams as a function of temperature T and cooling time $t_{\rm ff}$.[5] The difference in this scaling relation leads to two effects. First, for warm-hot ($T \gtrsim 10^5$ K) gas, since $t_{\rm cool}$ in MHD+ follows a steeper power ($\propto T^3$) law than CR+ ($\propto T^2$), gas in MHD+ generally has longer cooling time and thus stays at a higher temperature range than CR+. Secondly, for cool ($T \lesssim 10^5$ K) gas, since $t_{\rm cool} \propto T^{-1}$ in CR+, cooler gas has even longer cooling time, which allows gas to pile up at $T \sim 10^5$ K in CR+.

[5]We also checked phase diagrams at other radii; although the locations and shapes of the phase plot change due to radial dependence of density and temperature, the power-law scalings still hold at different radii.

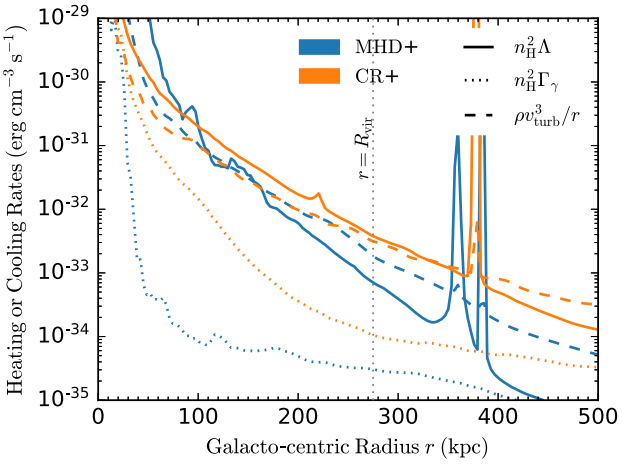

Figure 6. Volume-weighted radial profiles of cooling and heating rates in the inflow regions: radiative cooling $n_H^2\Lambda$ (*solid*), photon heating $n_H^2\Gamma_\gamma$ (*dotted*) and approximate turbulent heating $\rho v_{turb}^3/r$ (*dashed*, see details about this estimation in the text), for the MHD+ (blue) and CR+ (orange) runs of the m12i halo at $z = 0$. Turbulent heating could exceed radiative cooling at most radii in MHD+, while is a slightly subdominant inside R_{vir} in CR+. Photon heating is negligible in both MHD+ and CR+ runs.

In greater detail, we investigate how different phases of halo gas contribute to volume-integrated emissivity $n^2\Lambda$ in our MHD+ and CR+ runs. For MHD+, at large radii $r \gtrsim 150$ kpc, emissivity is dominated by hot, low-density volume-filling halo gas that cools slowly. While in the inner-CGM with $50\,\mathrm{kpc} < r < 150\,\mathrm{kpc}$, pressure-confined, high-density clumps and filaments with an overdensity of $\rho > 5\bar{\rho}(r)$ contributes to ∼80 per cent of total emissivity, only filling ∼ 5 per cent of the total inner-CGM volume. The rest ∼20 per cent emissivity comes from hot and diffuse halo gas with a volume-filling factor of ∼95 per cent. For CR+, emissivity is systematically higher than MHD+ by one order of magnitude, and is primarily contributed by gas sitting around $\rho \sim \rho_{eq}$. This is also somewhat reflected in Fig. 4, where both the magnitude and the dispersion of t_{cool} in MHD+ is greater than those in CR+.

In summary, the gas cooling process evolves differently: in MHD+, cooling gas condenses out into dense cold clumps, meaning that the volume-filling phase (relevant for virial shocks) is the reservoir of hot and low-density gas that cools relatively slowly. In contrast, cooler gas in CR+ can remain at intermediate temperatures with volume-filling densities. One might worry that our resolution is insufficient to accurately capture these phenomena (Hummels et al. 2019), but recent idealized simulations of the thermal instability in a patch of the CGM with CRs (Butsky et al. 2020) have demonstrated exactly the results above, when $P_{cr} \gg P_{thermal}$.

4.5 Heating terms

Fig. 6 shows volume-averaged profiles of selected cooling and heating rates for the m12i halo runs at $z = 0$: radiative cooling $n_H^2\Lambda$, photon heating $n_H^2\Gamma_\gamma$ and approximate turbulent heating[6] $\rho v_{turb}^3/r$. CR non-adiabatic heating (collisional + streaming) is negligible compared with gas cooling (Ji et al. 2020) and thus is not shown here. We find that in MHD+, turbulent heating could be larger than radiative cooling at $r \gtrsim 100$ kpc. In CR+, turbulent heating is a subdominant, but not totally negligible component compared to radiative cooling within a radius of $\lesssim$400 kpc. Therefore, even though t_{cool} is much shorter than t_{inflow} within R_{vir} in CR+ (as shown in the right-hand panel of Fig. 4), the inflowing gas does not cool to, but instead stays slightly above the photoionization equilibrium (PIE) temperature (fig. 7 in Ji et al. 2020) due to non-negligible turbulent heating. Photon heating is insignificant compared to gas cooling in both MHD+ and CR+ runs, as the halo gas is still away from PIE.

4.6 Halo mass and redshift dependence

4.6.1 Halo Mass

As discussed in Section 1, in classic virial shock models (ignoring feedback, turbulence, magnetic fields, CRs, and assuming spherical symmetry), one expects $t_{cool}/t_{ff} \sim (M_{vir}/10^{11}\,M_\odot)^\alpha$ with α between 1/3 and 2/3 at $r \sim R_{vir}$ (Silk 1977; Rees & Ostriker 1977), so hot haloes only form at high masses. We therefore extend our investigation to haloes of different masses. Fig. 7 shows visualizations of shocks, for four representative haloes of different mass, all at $z = 0$. Fig. 8 summarizes the estimates of t_{cool}/t_{inflow} around R_{vir} for all our simulations. We note that since the *volume-filling* phase of the CGM is the most relevant to our diagnosis of viral shocks, profiles of these timescales are *volume-averaged* values.

In our least massive haloes ($M_{vir} \ll 10^{11}\,M_\odot$, e.g. m10q), CRs have very weak effects, as the injection rates are low (owing to small galaxy masses) and the effects of mechanical feedback from supernovae are very strong in the shallow potential (this is shown in detail in Hopkins et al. (2020c) and Ji et al. (2020). Naively comparing the 'classic' virial model, it might be surprising that these haloes exhibit $t_{cool} \sim 10\,t_{ff}$ and clear shocks (with or without CRs), but these arise from that same strong stellar feedback[7] (the shocks are *outward*-propagating, owing to outflows from successive bursts of star formation, rather than virial shocks; see Hopkins et al. 2020a). At slightly higher masses (∼$10^{11}\,M_\odot$, e.g. m11b and m11i), we see CRs begin to have an effect on shock prominence, but the effect is weak.

Above $M_{vir} \gtrsim 10^{11.5}\,M_\odot$ (e.g. m11d, m11e, and m11f), the effects of CRs become prominent at ∼R_{vir}. The qualitative effects are similar to our m12i case study, albeit weaker. In MHD+, we see that while slightly lower mass $10^{11}\,M_\odot$ haloes have rapidly dropping t_{cool} inside R_{vir}, these haloes are indeed beginning to building up 'hot halo', with high central temperatures and $t_{cool} \sim 5\,t_{inflow} \sim 10\,t_{ff}$ for the hot volume-filling phase at outer CGM radii (at inner CGM radii gas remains cool, in $10^{11} - 10^{12}\,\mathrm{M}_\odot$ haloes, see Stern et al. 2020), and (as a consequence) a visible quasi-spherical virial shock emerges. In CR+, the combination of larger t_{inflow} and lower t_{cool} keeps $t_{cool} \sim t_{inflow}$ at $r \lesssim R_{vir}$. Around L_* ($M_{vir} \gtrsim 10^{12}\,\mathrm{M}_\odot$; e.g. m12i, m12m, and

[6]Turbulent heating here is estimated as turbulent energy density ρv_{turb}^2 dissipated over an eddy-turnover time r/v_{turb} at a length scale of r, assuming homogeneous and isotropic turbulence. These assumptions do not strictly apply in our simulations, which could lead us to overestimate the dissipation rate relative to a treatment which would account for gravitational stratification (e.g. Pouquet et al. 2017). In addition, this estimate actually includes all motion, even large-scale kinetic motion in the halo (e.g. 'eddies' of ∼100 kpc) in the halo as well. Therefore, the magnitude of turbulent heating quoted here is a rough estimate.

[7]Even without gas outflows, post-shock temperatures (at $z \sim 0$) in haloes of this mass are low, comparable to the equilibrium temperature between UVB heating and gas cooling and to the IGM gas temperature (see discussion in Kereš et al. 2005). Therefore, the stable shock criterion is satisfied in these objects even if strong shock from infall is not present.

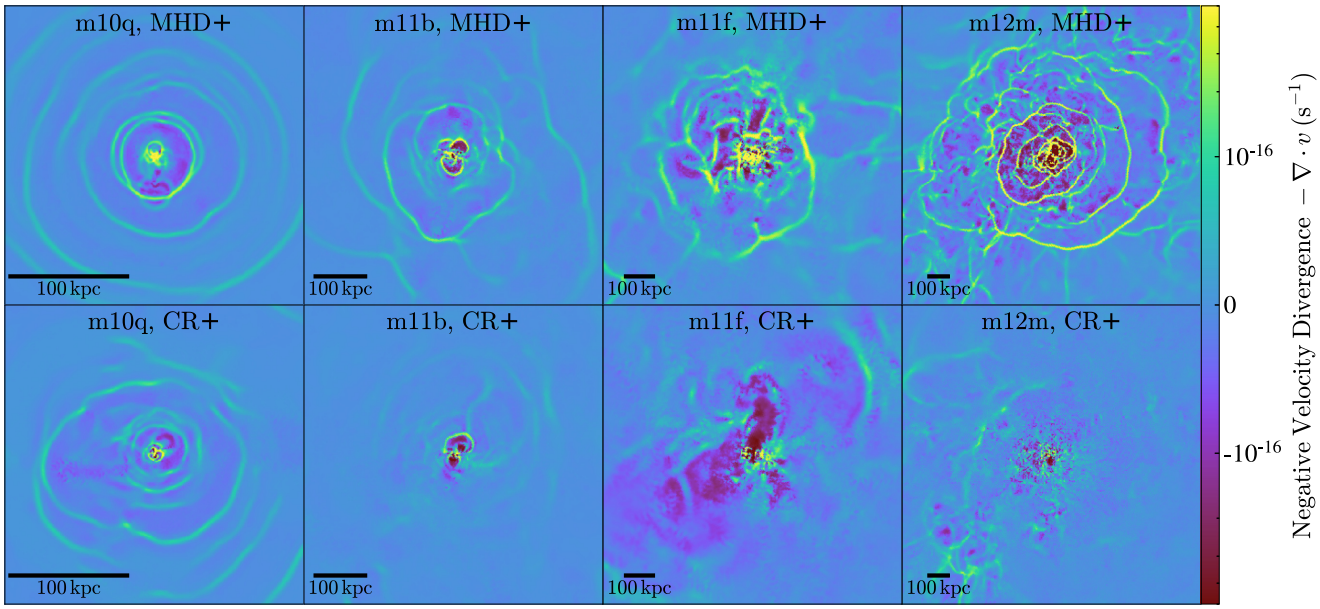

Figure 7. Slice plots edge-on to the disc of negative velocity divergences $-\nabla \cdot \boldsymbol{v}$ (as Fig. 1), in 'MHD+' (*top*) and 'CR+' (*bottom*) runs for m10q, m11b, m11f, and m12m haloes at $z = 0$. With increasing halo masses, shock features becomes more apparent in MHD+, but are more strongly suppressed in CR+. Note that shocks at **m10q** are not inflow/virial shocks, but outflow shocks from bursts of star formation feedback.

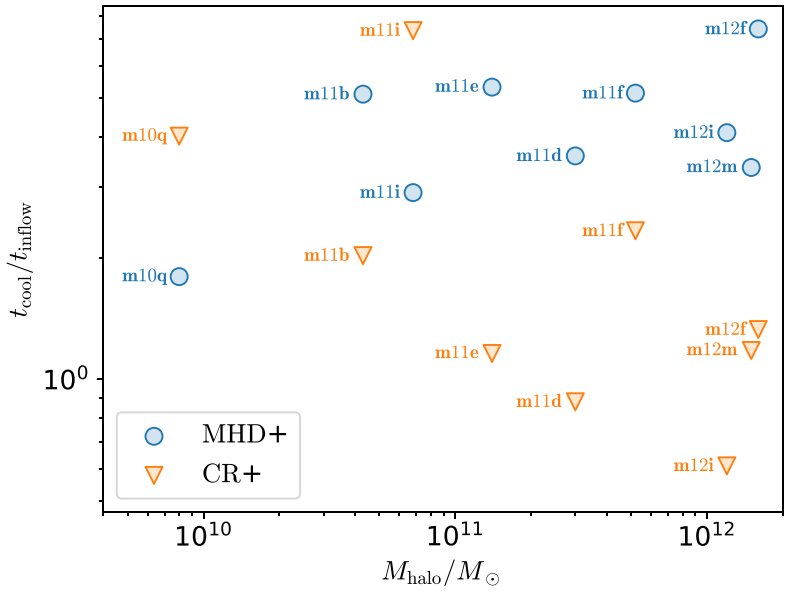

Figure 8. $t_{\rm cool}/t_{\rm inflow}$ versus $M_{\rm halo}$ measured at $r = R_{\rm vir}$ in various haloes with mass ranging from 10^{10} M$_\odot$ to 10^{12} M$_\odot$, for both MHD+ (*blue circles*) and CR+ (*orange triangles*) runs at $z = 0$. The CR+ runs have systematically lower $t_{\rm cool}/t_{\rm inflow}$ ratios than MHD+ in massive haloes, becoming chaotic in lower mass haloes where feedback from starburst activity is dominant and CR pressure effects are weak (see Hopkins et al. 2020c; Ji et al. 2020).

m12f), the relative effects of CRs in all cases resemble our m12i case study.

Notably, it appears that both the prominence of the hot gas in MHD+ and the CR pressure at $R_{\rm vir}$ in CR+ build up qualitatively similarly as galaxies become more massive (e.g. we see the radii out to which CRs have a strong effect, even *relative to* $R_{\rm vir}$, increases steadily with $M_{\rm vir}$). The former owes to the usual cooling physics above. The latter owes to the relative scaling of the efficiency of star formation (hence the amount of CR injection, $\dot{E}_{\rm cr}$) increasing in higher mass haloes.

We do not simulate higher mass haloes, because we do not include AGN feedback, and as a result above $M_{\rm vir} \gg 10^{12}$ M$_\odot$, these simulations exhibit severe overcooling and failure to quench (see e.g. Feldmann & Mayer 2015; Anglés-Alcázar et al. 2017; Feldmann et al. 2017; Parsotan et al. 2020; Wellons et al. 2020). However, we expect virial shocks to 'return' even in CR+ runs at higher masses. If the key criterion is that CR pressure dominate over thermal or accretion ram pressure at $\sim R_{\rm vir}$, then in the simple steady-state scalings from Hopkins et al. (2020c), this requires $\dot{E}_{\rm cr} \gtrsim C\, M_{\rm vir}/\tilde{\kappa}$ where C includes various constants. If SNe were the primary source

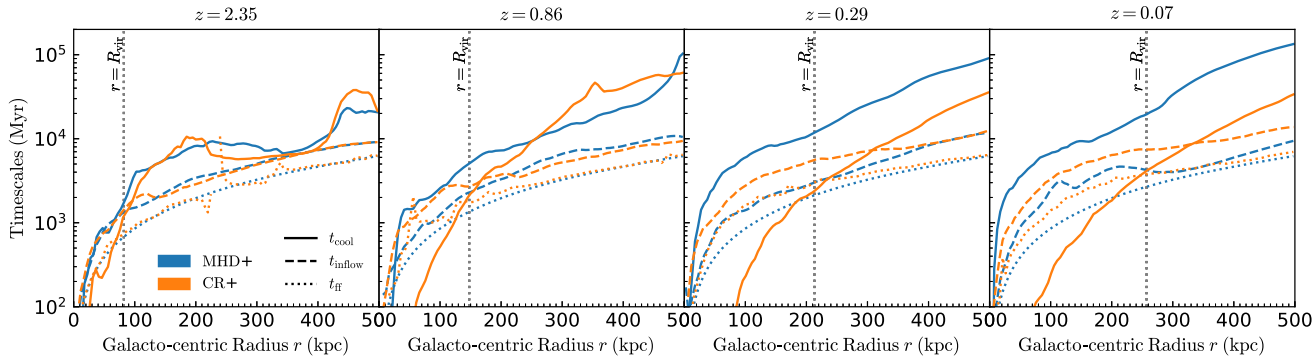

Figure 9. Volume-weighted radial profiles of various time-scales associated with inflows (as Fig. 4): cooling time $t_{\rm cool} = 3/2\,kT/n\Lambda$ (*solid*), inflow time $t_{\rm inflow} = r/v_{\rm inflow}$ (*dashed*), free-fall time $t_{\rm ff} = \sqrt{2r/(\nabla\Phi + \nabla P_{\rm cr}/\rho)}$ (*dotted*) in the MHD+ (*blue*), and CR+ (*orange*) runs of m12m haloes at different redshifts of 2.35, 0.86, 0.29, and 0.07 (where $z = 0$ is shown in Fig. 4), with the locations of $R_{\rm vir}$ marked with dotted vertical lines.

of CRs, and star formation were properly quenched as observed at $M_{\rm vir} \gtrsim 10^{12}\,{\rm M}_\odot$, then we would expect virial shocks to appear at masses $\gtrsim 10^{12.5}\,{\rm M}_\odot$ or so. However, AGN can of course also inject CRs. But because (at high masses) $M_{\rm BH} \propto M_* \propto M_{\rm vir}^{0.2}$ increases weakly with $M_{\rm vir}$, it is unlikely that even BHs at high Eddington ratios can lead to CRs dominating the pressure at $R_{\rm vir}$ in very massive haloes with $M_{\rm vir} \gg 10^{13}\,M_\odot$. This has been confirmed explicitly in recently simulations including AGN and CRs (e.g. Ruszkowski, Yang & Reynolds 2017; Su et al. 2019; Wang, Ruszkowski & Yang 2020).

4.6.2 *Redshift*

We next examine how the effect of CRs on virial shocks evolves over time for a representative halo m12i. As discussed in Hopkins et al. (2020c) and Ji et al. (2020), CR pressure is insufficient to balance against gravity and thus negligible at higher redshifts of $z \gtrsim 1$–2; therefore, it becomes particularly interesting how CR effects grow with time and affect the development of virial shocks. Fig. 9 shows the time evolution of radial profiles of cooling/inflow/free-fall times, and Fig. 10 shows visualizations of gas temperatures, velocity divergences as well as velocity streamlines in m12i at different redshifts.

At a higher redshift $z = 2.35$, no apparent difference in time-scales or temperature/velocity plots between MHD+ and CR+ is observed, since CR effects are still weak. At $z = 0.86$, CR pressure starts to build up in the inner-CGM with $r \lesssim 150$ kpc in the CR+ run, which leads to two consequences: (1) inflow time-scale increases since CRs provide pressure support and delay gas inflowing and (2) cooling time-scale becomes shorter than MHD+ since the volume-filling phase of gas is at lower T and higher $n_{\rm H}$, as discussed in Section 4.4, which corresponds to cooler inner-CGM in CR+ shown in the temperature plot. In the outer-CGM with $r \gtrsim 150$ kpc, shocks are prominent in both MHD+ and CR+ at this redshift, and raise $t_{\rm cool}$ by heating up halo gas. Note that these shocks are actually outflowing supernova shocks rather than virial shocks, which is clearly demonstrated by outward velocity streamlines near shock fronts in Fig. 10. SN shocks are slightly less violent in CR+ than MHD+ in terms of shock heating and distances travelled, since at this time SFR in CR+ run is already significantly lower than in MHD+ case so there is less SN energy available.

At a lower redshift $z = 0.29$, CR effects propagate towards larger radii $r \gtrsim 150$ kpc and become more substantial. $t_{\rm cool}$ in MHD+ grows significantly from its high-redshift values, in contrast to the CR+ case where the volume-filling phase dominated by CR pressure is at higher $n_{\rm H}$ and lower T, and thus $t_{\rm cool}$ is lower. $t_{\rm inflow}$ in CR+ is also boosted by CR pressure support, while in MHD+ $t_{\rm inflow}$ is systematically smaller due to the lack of pressure support. At this stage, the ratio $t_{\rm cool}/t_{\rm inflow}$ becomes less than 1 in CR+ for $r \lesssim 350$ kpc, and inflowing gas cools efficiently and feeds the central galaxy gently along the galactic plane, without creating any prominent shock. CR-driven outflows also start to develop in the bi-conical regions. In MHD+, $t_{\rm cool}$ of the volume-filling phase is always greater than $t_{\rm inflow}$ throughout the halo, and thus relatively hot gas with long cooling time and insufficient pressure support continues to fall in and generates virial shocks, building up a hot halo with a radius of $\sim$100 kpc at $z = 0.29$. This hot, virialized halo continues to grow in size, reaching a radius of $\sim$200 kpc at $z = 0.07$ and $\sim$300 kpc at $z = 0$ (Fig. 1); $t_{\rm cool}$ and $t_{\rm inflow}$ are further raised, respectively, by higher gas temperatures and greater thermal pressure gradients due to virial shock heating in MHD+.

In short, at higher redshifts $z \gtrsim 2$, there exists very little difference between MHD+ and CR+, and starburst activity is the governing process that determines kinematics and thermal states of halo gas. With deceasing redshifts, CR effects become increasingly more important and develop from the inside out, reducing $t_{\rm cool}$ by modifying phases of inflowing gas and raising $t_{\rm inflow}$ by providing CR pressure support, and thus virial shocks are almost invariably suppressed in our MW-mass CR+ runs.

5 CONCLUSIONS AND DISCUSSIONS

We explore the effects of CRs on the formation of virial shocks and 'hot haloes' in galaxies up to $\sim 10^{12}\,{\rm M}_\odot$, in cosmological zoom-in simulations including star formation, cooling, magnetic fields, conduction, viscosity, and (optionally) explicit transport and gas coupling between CRs and gas.

Absent CRs, we show that $\gtrsim 10^{11}\,{\rm M}_\odot$ haloes at low redshifts exhibit clear, quasi-spherical virial shocks at $r \sim R_{\rm vir}$. Within the virial shock, inflows become well-mixed with thermal-pressure-driven confined outflows, and a classic cooling flow emerges: cooling times of the volume-filling phase are longer than infall times, infall is subsonic, temperatures and densities increase towards $r \to 0$. Gas at a given galacto-centric radius is in approximate thermal pressure equilibrium (so cool gas is highly overdense).

With CRs as modeled here (under certain assumptions including a streaming speed at $v_{\rm A}$ and a constant diffusion coefficient), the virial shocks are absent or vastly weaker in $\sim L_*$ haloes when CR pressure dominates over thermal pressure around $\sim R_{\rm vir}$. Inflows develop a simple structure which we show can be analytically predicted assuming a steady-state, spherical, CR-pressure-dominated

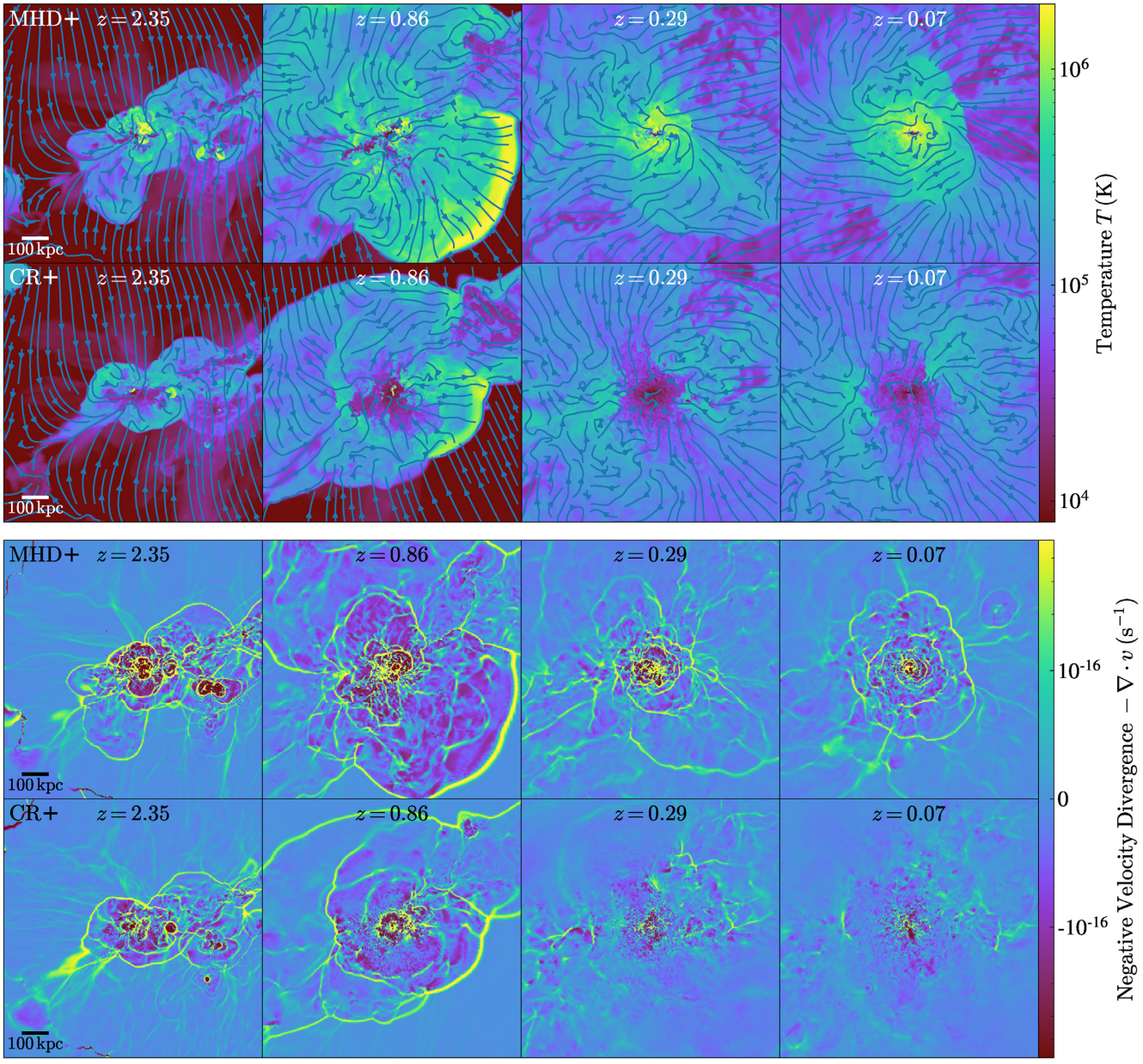

Figure 10. Slice plots edge-on to the disc of temperatures T (with velocity streamlines superposed) and negative velocity divergences $-\nabla \cdot \boldsymbol{v}$ (as Fig. 1), in 'MHD+' (*top*) and 'CR+' (*bottom*) runs for m12i halo at different redshifts of 2.35, 0.86, 0.29, and 0.07 ($z = 0$ is shown in Fig. 1). At higher redshifts, both MHD+ and CR+ have strong outflowing supernova shocks that collide with inflowing gas and heat up the CGM. However, at lower redshifts, MHD+ develops a hot halo growing in size with strong virial shocks, while in CR+, a cooler halo forms with much less apparent shocks, when CR pressure gradually becomes dominant in the CGM.

halo. Inflows are approximately isothermal, with constant subsonic inflow velocity, and gas is not in local thermal pressure equilibrium but rather in *total* pressure equilibrium with CRs constituting most of the pressure. Our analytic model also predicts the ratio of inflow and outflow densities, velocities, and mass fluxes. In this limit, overdense gas sinks while underdense gas is accelerated outwards, while temperatures are largely set by external heating, so inflows are actually more dense and have larger thermal pressure compared to outflows. Outflows have slightly higher velocity while inflows carry slightly larger mass flux, but the difference is small (tens of per cent), where it can be very large absent CRs.

This difference emerges as follows: absent CRs, as a halo grows over time, its virial temperature and velocity evolve only weakly, but as the virial radius $R_{\rm vir}$ expands and the mean density of the universe drops, and warm/cool gas which is thermally unstable precipitates out into overdense clumps, the mean gas density ρ of the remaining, inflowing gas at $\gtrsim R_{\rm vir}$ drops[8] and the cooling time $t_{\rm cool}(r \sim R_{\rm vir})$ grows until $t_{\rm cool} > t_{\rm inflow}$ at $\sim R_{\rm vir}$ and a stable virial shock forms with a hot halo interior. CRs modify this in many ways, but we show the most important are (1) the additional CR pressure can directly support a large weight of gas with low thermal pressure, and (2) the *lack* of local thermal pressure equilibrium means cooler gas can

[8]Note we obtain the same scalings if we consider turnaround or splashback radii, as these scales similar to $R_{\rm vir}$.

Table 1. Zoom-in simulation volumes run to $z = 0$ (see Hopkins et al. 2018 for details). All units are physical.

Simulation name	$M_{\rm halo}^{\rm vir}$ [$M_\odot$]	$M_*^{\rm MHD+}$ [$M_\odot$]	$M_*^{\rm CR+}$ [$M_\odot$]	$m_{i,\,1000}$ [$1000\,M_\odot$]	$\langle\epsilon_{\rm gas}\rangle^{\rm sf}$ [pc]	Notes
m10q	8.0e9	2e6	2e6	0.25	0.8	Isolated dwarf in an early-forming halo
m11b	4.3e10	8e7	8e7	2.1	1.6	Discy (rapidly-rotating) dwarf
m11e	1.4e11	1e9	7e8	7.0	2.0	Low surface-brightness dwarf
m11d	3.3e11	4e9	2e9	7.0	2.1	Late-forming, 'fluffy' halo and galaxy
m11f	5.2e11	3e10	1e10	12	2.6	Early-forming, intermediate-mass halo
m12i	1.2e12	7e10	3e10	7.0	2.0	'Latte' halo, later-forming MW-mass halo, massive disc
m12m	1.5e12	1e11	3e10	7.0	2.3	Earlier-forming halo, features strong bar at late times
m12f	1.6e12	8e10	4e10	7.0	1.9	MW-like disc, merges with LMC-like companion

Note. Halo/stellar properties listed refer only to the original 'target' halo around which the high-resolution volume is centred: these volumes can reach up to $\sim$(1–10 Mpc)^3 comoving, so there are actually several hundred resolved galaxies in total. (1) Simulation name: Designation used throughout this paper. (2) $M_{\rm halo}^{\rm vir}$: Virial mass (following Bryan & Norman 1998) of the 'target' halo at $z = 0$. (3) $M_*^{\rm MHD+}$: Stellar mass of the central galaxy at $z = 0$, in our non-CR, but otherwise full-physics ('MHD+') run. (4)$M_*^{\rm CR+}$: Stellar mass of the central galaxy at $z = 0$, in our 'default' (observationally favoured) CR+ ($\kappa = 3e29$) run. (5)$m_{i,\,1000}$: Mass resolution: The baryonic (gas or star) particle/element mass, in units of $1000\,M_\odot$. The DM particle mass is always larger by the universal ratio, a factor of $\approx$5. (6) $\langle\epsilon_{\rm gas}\rangle^{\rm sf}$: Spatial resolution: The gravitational force softening (Plummer-equivalent) at the mean density of star formation (gas softenings are adaptive and match the hydrodynamic resolution, so this varies) in the MHD+ run. Typical time resolution reaches $\sim$100–100 yr, density resolution $\sim10^3$–10^4 cm^{-3}. (7) Additional notes.

be volume-filling and is not compressed into dense clumps. This allows more (factor $\sim$a few higher $\sim M_{\rm gas}(<r)$ and $\rho(r)$) cooler ($\sim10^5$ K) gas to remain at $r\sim R_{\rm vir}$, giving rise to order-of-magnitude shorter cooling times $t_{\rm cool}$ at $\sim R_{\rm vir}$. This maintains $t_{\rm cool}\lesssim t_{\rm inflow}$ within $\sim R_{\rm vir}$, suppressing the formation of a stable virial shock and hot halo.

From the above, we see CRs do not 'erase' virial shocks: rather, their effect is to *delay* their formation until galaxies reach later times/larger mass scales. The key criterion for CRs to have this effect is that CR pressure dominates over thermal and accretion/ram pressure at $\sim R_{\rm vir}$. This becomes more challenging in higher-mass haloes and at higher redshifts, in our simple steady-state model requiring an injection rate $\dot{E}_{\rm cr}\propto M_{\rm vir}\,(1+z)^3/\tilde{\kappa}$. Knowing that star formation is largely quenched in galaxies above $M_{\rm vir}\gtrsim10^{12}\,M_\odot$, even invoking AGN (with $M_{\rm BH}\propto M_*\propto M_{\rm vir}^{0.2}$ as observed at high masses), CR most likely can only 'delay' the onset of the hot halo until $M_{\rm vir}\sim10^{13}\,M_\odot$ at $z\sim0$ (with a smaller effect at higher z), assuming galaxies remain star forming and provide source of CRs (however most of the observed galaxies are passive in this mass range so our model does not strictly apply).

Since the thermal state of halo gas in the CR+ runs is quite distinct from MHD+, we expect dramatically different observables from our CR and non-CR runs. In addition to ion column densities that are discussed extensively in Ji et al. (2020), we also find different X-ray emissions between MHD+ and CR+. Within a radius of 200 kpc in m12i, the volume-integrated soft (0.5–2 keV) X-ray luminosity is $\sim4\times10^{39}$ erg s^{-1} in MHD+ and $\sim6.7\times10^{38}$ erg s^{-1} in CR+, respectively; both of these two values are quite consistent with observations by Li, Crain & Wang (2014) (given SFR and $M_\star$ in CR+ is a factor of $\sim$3 smaller than MHD+, Table 1) and qualitatively similar to previous FIRE-1 results (van de Voort et al. 2016). We note that compared to MHD+, the soft X-ray emission from the CGM (with the central galaxy excluded) in CR+ is significantly less: the X-ray emission mainly comes from inflows along the galactic plane, where the CR pressure is less dominant and thus the gas is warmer compared to the bi-conical outflows. In contrast, the MHD+ run produces a halo with volume-filling X-ray emissions. We leave detailed comparisons on X-ray emissions and the SZ effect between MHD+ and CR+ for future study.

We emphasize, however, our conclusions could be altered by a number of physical uncertainties, in particular, the uncertainty in CR transport physics. As discussed in Chan et al. (2019) and Hopkins et al. (2020c), we deploy a constant CR diffusion coefficient (with a streaming speed at the Alfvén speed $v_{\rm A}$) which is calibrated by CR population modeling in the MW and gamma-ray observations in nearby galaxies. However, there is no observational constraint on CR population in the CGM, and it is plausible that the CR diffusion coefficient is a complicated function of local gas properties, such as number densities, ionization fractions, magnitudes, and morphologies of magnetic fields, turbulence, etc. (see e.g. a review paper Zweibel 2013). For instance, when CRs enter the CGM where gas number densities, magnitudes of magnetic fields and strengths of turbulence are lower, CRs might become less confined and escape from galaxy haloes more quickly than what we see in our CR+ runs. In Hopkins et al. (2020b) we have already shown that observationally allowed diffusion coefficients that scales with physical properties of the gas typically leads to properties of galaxies intermediate between MHD and CR+. As a consequence, the level of CR pressure dominance in the CGM and the impact of CRs on the formation of virial shocks in our simulations might change with more realistic CR transport treatments. In addition, CRs can also be potentially produced or re-accelerated by shocks via the second-order Fermi process (Fermi 1949), which might change the CR abundance in the CGM and modify our conclusions, and we did not include this process as a possible CR source in our simulations. We leave these caveats for future study.

ACKNOWLEDGEMENTS

We thank the referee Mateusz Ruszkowski for constructive and insightful suggestions. SJ is supported by a Sherman Fairchild Fellowship from Caltech. TKC is supported by Science and Technology Facilities Council (STFC) astronomy consolidated grant no. ST/T000244/1. Support for PFH and co-authors was provided by an Alfred P. Sloan Research Fellowship, NSF Collaborative Research grant no. 1715847 and CAREER grant no. 1455342, and NASA grant nos NNX15AT06G, JPL 1589742, and 17-ATP17-0214. DK was supported by NSF grant no. AST-1715101 and the

Cottrell Scholar Award from the Research Corporation for Science Advancement. CAFG was supported by NSF through grant no. AST-1715216 and CAREER award AST-1652522, by NASA through grant no. 17-ATP17-0067, by STScI through grant nos *HST*-GO-14681.011, *HST*-GO-14268.022-A, and *HST*-AR-14293.001-A, and by a Cottrell Scholar Award from the Research Corporation for Science Advancement. Numerical calculations were run on the Caltech compute cluster 'Wheeler', allocations from XSEDE TG-AST120025, TG-AST130039 and PRAC NSF.1713353 supported by the NSF, and NASA HEC SMD-16-7592. The data used in this work here were, in part, hosted on facilities supported by the Scientific Computing Core at the Flatiron Institute, a division of the Simons Foundation. We have made use of NASA's Astrophysics Data System. Data analysis and visualization are made with PYTHON 3, and its packages including NUMPY (Van Der Walt, Colbert & Varoquaux 2011), SCIPY (Oliphant 2007), MATPLOTLIB (Hunter 2007), and the YT astrophysics analysis software suite (Turk et al. 2010), as well as the spectral simulation code CLOUDY (Ferland et al. 2017).

DATA AVAILABILITY

The data supporting the plots within this article are available on reasonable request to the corresponding author. A public version of the GIZMO code is available at http://www.tapir.caltech.edu/~phopkins/Site/GIZMO.html.

Additional data including simulation snapshots, initial conditions, and derived data products are available at http://fire.northwestern.edu.

REFERENCES

Anderson M. E., Bregman J. N., 2011, ApJ, 737, 22
Anderson M. E., Churazov E., Bregman J. N., 2015, MNRAS, 452, 3905
Anglés-Alcázar D., Faucher-Giguère C.-A., Quataert E., Hopkins P. F., Feldmann R., Torrey P., Wetzel A., Kereš D., 2017, MNRAS, 472, L109
Birnboim Y., Dekel A., 2003, MNRAS, 345, 349
Brooks A., Governato F., Quinn T., Brook C., Wadsley J., 2009, ApJ, 694, 396
Bryan G. L., Norman M. L., 1998, ApJ, 495, 80
Buck T., Pfrommer C., Pakmor R., Grand R. J., Springel V., 2020, MNRAS, 497, 1712
Burchett J. N. et al., 2019, ApJ, 877, L20
Butsky I. S., Fielding D. B., Hayward C. C., Hummels C. B., Quinn T. R., Werk J. K., 2020, AJ, 903
Cai Z. et al., 2017, ApJ, 839, 131
Cantalupo S., Arrigoni-Battaia F., Prochaska J. X., Hennawi J. F., Madau P., 2014, Nature, 506, 63
Chan T., Kereš D., Hopkins P., Quataert E., Su K., Hayward C., Faucher-Giguère C., 2019, MNRAS, 488, 3716
Dekel A., Birnboim Y., 2006, MNRAS, 368, 2
Dijkstra M., Loeb A., 2009, MNRAS, 400, 1109
Esmerian C. J., Kravtsov A. V., Hafen Z., Faucher-Giguere C.-A., Quataert E., Stern J., Keres D., Wetzel A., 2020, MNRAS, preprint (arXiv:2006.13945)
Fall S. M., Efstathiou G., 1980, MNRAS, 193, 189
Fang T., Bullock J., Boylan-Kolchin M., 2012, ApJ, 762, 20
Farber R., Ruszkowski M., Yang H.-Y., Zweibel E., 2018, ApJ, 856, 112
Fardal M. A., Katz N., Gardner J. P., Hernquist L., Weinberg D. H., Davé R., 2001, ApJ, 562, 605
Faucher-Giguère C.-A., Kereš D., 2011, MNRAS, 412, L118
Faucher-Giguere C.-A., Lidz A., Zaldarriaga M., Hernquist L., 2009, ApJ, 703, 1416
Faucher-Giguère C.-A., Kereš D., Dijkstra M., Hernquist L., Zaldarriaga M., 2010, ApJ, 725, 633
Faucher-Giguère C.-A., Kereš D., Ma C.-P., 2011, MNRAS, 417, 2982
Faucher-Giguere C.-A., Hopkins P. F., Kereš D., Muratov A. L., Quataert E., Murray N., 2015, MNRAS, 449, 987
Faucher-Giguere C.-A., Feldmann R., Quataert E., Kereš D., Hopkins P. F., Murray N., 2016, MNRAS, 461, L32
Feldmann R., Mayer L., 2015, MNRAS, 446, 1939
Feldmann R., Quataert E., Hopkins P. F., Faucher-Giguère C.-A., Kereš D., 2017, MNRAS, 470, 1050
Ferland G. et al., 2017, preprint (arXiv:1705.10877)
Fermi E., 1949, Phys. Rev., 75, 1169
Fielding D., Quataert E., McCourt M., Thompson T. A., 2017, MNRAS, 466, 3810
Fumagalli M., Prochaska J. X., Kasen D., Dekel A., Ceverino D., Primack J. R., 2011, MNRAS, 418, 1796
Guo F., Oh S. P., 2008, MNRAS, 384, 251
Hafen Z. et al., 2017, MNRAS, 469, 2292
Hennawi J. F., Prochaska J. X., Cantalupo S., Arrigoni-Battaia F., 2015, Science, 348, 779
Hernquist L., 1990, ApJ, 356, 359
Hollenbach D., McKee C. F., 1979, ApJS, 41, 555
Hopkins P. F. et al., 2018, MNRAS, 480, 800
Hopkins P. F. et al., 2020c, MNRAS, 492, 3465
Hopkins P. F., 2015, MNRAS, 450, 53
Hopkins P. F., 2016, MNRAS, 462, 576
Hopkins P. F., 2017, MNRAS, 466, 3387
Hopkins P. F., Raives M. J., 2016, MNRAS, 455, 51
Hopkins P. F., Kereš D., Oñorbe J., Faucher-Giguère C.-A., Quataert E., Murray N., Bullock J. S., 2014, MNRAS, 445, 581
Hopkins P. F., Chan T., Ji S., Hummels C., Keres D., Quataert E., Faucher-Giguère C.-A., 2020a, MNRAS, 501, 3640
Hopkins P. F., Squire J., Chan T., Quataert E., Ji S., Keres D., Faucher-Giguère C.-A., 2020b, MNRAS, 501, 4184
Hummels C. B. et al., 2019, ApJ, 882, 156
Hunter J. D., 2007, Comput. Sci. Eng., 9, 90
Ji S. et al., 2020, MNRAS, 496, 4221
Ji S., Oh S. P., McCourt M., 2018, MNRAS, 476, 852
Jiang Y.-F., Oh S. P., 2018, ApJ, 854, 5
Kereš D., Hernquist L., 2009, ApJ, 700, L1
Kereš D., Katz N., Weinberg D. H., Davé R., 2005, MNRAS, 363, 2
Kereš D., Katz N., Fardal M., Davé R., Weinberg D. H., 2009, MNRAS, 395, 160
Li J.-T., Li Z., Wang Q. D., Irwin J. A., Rossa J., 2008, MNRAS, 390, 59
Li J.-T., Crain R. A., Wang Q. D., 2014, MNRAS, 440, 859
Martin C. L., Dijkstra M., Henry A., Soto K. T., Danforth C. W., Wong J., 2015, ApJ, 803, 6
McKenzie J. F., Voelk H. J., 1982, A&A, 116, 191
Navarro J. F., Frenk C. S., White S. D. M., 1996, ApJ, 462, 563
Nelson D. et al., 2019, MNRAS, 490, 3234
Nelson D., Vogelsberger M., Genel S., Sijacki D., Kereš D., Springel V., Hernquist L., 2013, MNRAS, 429, 3353
Ocvirk P., Pichon C., Teyssier R., 2008, MNRAS, 390, 1326
Oliphant T. E., 2007, Comput. Sci. Eng., 9, 10
Oppenheimer B. D., Davé R., Kereš D., Fardal M., Katz N., Kollmeier J. A., Weinberg D. H., 2010, MNRAS, 406, 2325
Parsotan T., Cochrane R., Hayward C., Angles-Alcazar D., Feldmann R., Faucher-Giguere C.-A., Wellons S., Hopkins P., 2020, MNRAS, 501, 1591
Planck Collaboration et al., 2013, A&A, 557, A52
Pouquet A., Rosenberg D., Marino R., Herbert C., 2017, Journal of Fluid Mechanics, 844, 519
Prochaska J. X. et al., 2017, ApJ, 837, 169
Qu Z., Bregman J. N., 2019, ApJ, 880, 89
Rees M. J., Ostriker J., 1977, MNRAS, 179, 541
Ruszkowski M., Yang H.-Y. K., Reynolds C. S., 2017, ApJ, 844, 13
Salem M., Bryan G. L., Corlies L., 2016, MNRAS, 456, 582
Silk J., 1977, ApJ, 211, 638
Sravan N. et al., 2016, MNRAS, 463, 120
Stern J. et al., 2020, AJ, 911, 25

Stern J., Hennawi J. F., Prochaska J. X., Werk J. K., 2016, ApJ, 830, 87
Stern J., Faucher-Giguère C.-A., Hennawi J. F., Hafen Z., Johnson S. D., Fielding D., 2018, ApJ, 865, 91
Stocke J. T., Keeney B. A., Danforth C. W., Shull J. M., Froning C. S., Green J. C., Penton S. V., Savage B. D., 2013, ApJ, 763, 148
Su K.-Y. et al., 2019, MNRAS, 487, 4393
Su K.-Y., Hopkins P. F., Hayward C. C., Faucher-Giguère C.-A., Kereš D., Ma X., Robles V. H., 2017, MNRAS, 471, 144
Tumlinson J., Peeples M. S., Werk J. K., 2017, ARA&A, 55, 389
Turk M. J., Smith B. D., Oishi J. S., Skory S., Skillman S. W., Abel T., Norman M. L., 2010, ApJS, 192, 9
Van Der Walt S., Colbert S. C., Varoquaux G., 2011, Comput. Sci. Eng., 13, 22
van de Voort F., Schaye J., 2013, MNRAS, 430, 2688
van de Voort F., Schaye J., Booth C., Haas M. R., Dalla Vecchia C., 2011, MNRAS, 414, 2458
van de Voort F., Quataert E., Hopkins P. F., Faucher-Giguère C.-A., Feldmann R., Kereš D., Chan T., Hafen Z., 2016, MNRAS, 463, 4533
van de Voort F., Bieri R., Pakmor R., Gómez F. A., Grand R. J., Marinacci F., 2020, MNRAS, 501, 4888
Wang C., Ruszkowski M., Yang H. K., 2020, MNRAS, 493, 4065
Wellons S., et al., 2020, MNRAS, 497, 4051
Werk J. K. et al., 2014, ApJ, 792, 8
White S. D., Rees M. J., 1978, MNRAS, 183, 341
Zweibel E. G., 2013, Phys. Plasmas, 20, 055501

This paper has been typeset from a TEX/LATEX file prepared by the author.